J. Fluid Mech. (2010), *vol.* 643, *pp.* 233–266. © Cambridge University Press 2009
doi:10.1017/S002211200999200X

Large eddy simulation of a stratified boundary layer under an oscillatory current

BISHAKHDATTA GAYEN[1], SUTANU SARKAR[1]† AND JOHN R. TAYLOR[2]

[1]Mechanical and Aerospace Engineering, University of California, San Diego, La Jolla, CA 92093, USA

[2]Earth and Planetary Sciences, Massachusetts Institute of Technology, Cambridge, MA 02139, USA

(Received 31 March 2009; revised 4 September 2009; accepted 4 September 2009;
first published online 17 December 2009)

A numerical study based on large eddy simulation is performed to investigate a bottom boundary layer under an oscillating tidal current. The focus is on the boundary layer response to an external stratification. The thermal field shows a mixed layer that is separated from the external stratified fluid by a thermocline. The mixed layer grows slowly in time with an oscillatory modulation by the tidal flow. Stratification strongly affects the mean velocity profiles, boundary layer thickness and turbulence levels in the outer region although the effect on the near-bottom unstratified fluid is relatively mild. The turbulence is asymmetric between the accelerating and decelerating stages. The asymmetry is more pronounced with increasing stratification. There is an overshoot of the mean velocity in the outer layer; this jet is linked to the phase asymmetry of the Reynolds shear stress gradient by using the simulation data to examine the mean momentum equation. Depending on the height above the bottom, there is a lag of the maximum turbulent kinetic energy, dissipation and production with respect to the peak external velocity and the value of the lag is found to be influenced by the stratification. Flow instabilities and turbulence in the bottom boundary layer excite internal gravity waves that propagate away into the ambient. Unlike the steady case, the phase lines of the internal waves change direction during the tidal cycle and also from near to far field. The frequency spectrum of the propagating wave field is analysed and found to span a narrow band of frequencies clustered around 45°.

Key words: simulation, stratified flows

1. Introduction

At the bottom of the ocean, a turbulent mixed layer develops as near-bottom currents flow over the sea floor. These currents are often oscillatory, for example, barotropic and internal tides, surface and internal gravity waves, inertial oscillations. The complex interplay of time-dependent currents, rotation, stratification and bottom topography determines the properties of the bottom boundary layer. The present large eddy simulation (LES) of a boundary layer on a flat non-sloping bottom under an oscillating current in a uniformly stratified fluid is designed to focus on the interaction of stratification and oscillation in the absence of other complicating factors. The following literature survey shows that this fundamental problem, especially the phase-dependent aspects, is not well understood.

---

† Email address for correspondence: ssarkar@ucsd.edu

In the context of oscillatory flows, it is useful to distinguish between pulsatile flows with non-zero mean and purely oscillatory flows with zero mean; the latter is the subject of the present work. For oscillatory flow over a smooth surface, the Reynolds number, $Re_s = U_0\delta_s/\nu$ based on the Stokes thickness, $\delta_s = \sqrt{2\nu/\omega}$, where ω is the tidal frequency, and peak external velocity U_0 is often used to classify the flow into qualitatively different regimes. Previous investigators such as Hino, Sawamoto & Takasu (1976), Hino *et al.* (1983), Sleath (1987) Jensen, Sumer & Fredsøe (1989), Akhavan, Kamm & Shapiro (1991*a*) and Sarpkaya (1993) have distinguished four different flow regimes for the unstratified zero time-mean oscillatory boundary layer based on the value of Reynolds number Re_s: (i) laminar flow when $Re_s < 100$; (ii) disturbed laminar flow for $100 < Re_s < 550$, where good agreement between velocity traces and laminar theory is found except during the accelerating phase of the cycle; (iii) intermittently turbulent (IT) flow for $Re_s > 550$, where turbulent bursts appear and three-dimensional nature of the turbulence is visible in contrast to the earlier two-dimensional behaviour in the disturbed laminar regime (for further details consult Blondeaux & Seminara 1979; Vittori & Verzicco 1998; Akhavan, Kamm & Shapiro 1991*b*) and (iv) fully turbulent (FT) flow at sufficiently large Reynolds number. While Re_s must be quite large for turbulence to persist throughout the entire cycle, Jensen *et al.* (1989) and Salon, Armenio & Crise (2007) found that turbulence is present for most of the cycle when Re_s is approximately 1800 or larger.

Unstratified oscillating flow has been the subject of numerical studies as summarized below. Direct numerical simulation (DNS) studies (e.g. Spalart & Baldwin 1987; Akhavan *et al.* 1991*b*; Vittori & Verzicco 1998; Costamagna, Vittori & Blondeaux 2003; Sakamoto & Akitomo 2008, their case of pure oscillation) have primarily studied the disturbed laminar and IT flow regimes. Spalart & Baldwin (1987) performed DNS of oscillating Stokes flow over a range of Reynolds numbers up to $Re_s = 1200$, observed a change from disturbed laminar to intermittent turbulence when $Re_s = 600$–800, identified a log-law over a portion of the cycle at $Re_s = 1200$, and proposed a new algebraic turbulence model. Akhavan *et al.* (1991*b*) in their DNS study of oscillating flow in a channel focused on transition to turbulence and explained features of the transition process observed in their laboratory experiment (Akhavan *et al.* 1991*a*) as a secondary instability of two-dimensional Tollmein–Schlichting waves. Vittori & Verzicco (1998) performed DNS in the disturbed laminar and the IT regime taking wall imperfections into account. They found that wall imperfections induce transition to turbulence and have a strong effect on the time evolution of the turbulent kinetic energy (TKE) in the disturbed laminar regime. Costamagna *et al.* (2003) have examined the role of coherent boundary layer structures in their DNS of the IT regime, and identify instability of low-speed streaks as important for the generation and the sustenance of turbulence in oscillating Stokes flow.

LES has been used recently to extend the scope to higher Reynolds numbers where the FT regime applies. LES has been shown to handle turbulence where there is a transition from laminar flow to turbulence in pulsating flows, for example, by Scotti & Piomelli (2001). The problem of purely oscillatory boundary layers has been studied with LES recently by Hsu, Lu & Kwan (2000), Lohmann *et al.* (2006), Salon *et al.* (2007) and Radhakrishnan & Piomelli (2008). Hsu *et al.* (2000) performed LES for Reynolds numbers up to $Re_s = 894$ that corresponds to the IT regime using a subgrid eddy viscosity model with the dynamic procedure, and a Reynolds-averaged Navier–Stokes (RANS) calculation of both the IT and FT regime that employed a $k - \omega$ model. Their simulations captured the transition from disturbed laminar to IT regime, and showed that the phase advance of peak shear stress with respect to peak velocity changed from its laminar value of 45° to about 10° in the IT regime. Lohmann *et al.* (2006) simulated a case with $Re_s = 3464$ in the FT region with LES using the standard Smagorinsky subgrid scale (SGS) model. Their results for temporal evolution of the wall shear stress and first- and second-order statistics did not reproduce the experimental results found by Jensen *et al.* (1989) in their test case 10 at the same Reynolds number. The discrepancy illustrates the unsuitability of the simple Smagorinsky SGS model for unsteady flow problems. Salon *et al.* (2007) preformed LES using the dynamic mixed model (DMM). The authors studied a case with $Re_s = 1790$, reproduced the experimental results of test case 8 by Jensen *et al.* (1989), and provided insight into the phase dependent variation of near-wall and outer-layer turbulence over a complete cycle. Recently, Radhakrishnan & Piomelli (2008) have performed LES with various subgrid models and near-wall treatments for simulations in the FT regime. The experimental results by Jensen *et al.* (1989) of test cases 10 ($Re_s = 3464$) and 13 (same flow conditions as test case 10 but with a rough wall) were successfully matched. These authors demonstrate the superiority of the dynamic Smagorinsky model over the standard one as well as the necessity of an additional wall layer model if the eddies responsible for near-wall turbulence are unresolved.

DNS and LES studies of an oscillating boundary layer subject to stratification are scarce. Sakamoto & Akitomo (2006) and Sakamoto & Akitomo (2009) report a DNS of a stratified tidal bottom Ekman layer for various values of the Rossby number Ro. The case of pure oscillation ($Ro = \infty$) in the study by Sakamoto & Akitomo (2009) was at $Re_s = 1000$, and all cases had a weak stratification, $N_\infty^2/\omega^2 = 47.5$. The authors mainly focused on the mixed layer growth along with energy transfer between potential and kinetic energy. They also studied the applicability of different turbulent scales for the mixed and the interfacial layers. There have also been studies of stratified tidal boundary layers using the RANS equations, for example, by Richards (1982), Davies, Jones & Xing (1997), Burchard, Petersen & Rippeth (1998). Calculations using the RANS equations typically require additional models, for example, stability functions based on Richardson number, to incorporate stability effects.

Burchard *et al.* (1998) report observations at a location in the Irish Sea that show a lag of dissipation rate with respect to the current. Lorke *et al.* (2002) in their measurements in a stratified basin under a low-speed oscillating flow also observed a lag in the dissipation rate with respect to the free-stream current. The authors also found a considerable difference between the dissipation rate estimated from the law of wall and that obtained using microstructure measurements. Thorpe *et al.* (2008) observe a lag of dissipation with respect to the tidal velocity at a location in the Irish Sea (water depth 43.5 m). They also observe upward propagating bursts that reach the surface to form boils. Measurements in the stratified boundary layer over the Oregon shelf have been employed to ascertain the effect of stratification on the log-law by Perlin *et al.* (2005) and on Ekman veering by Perlin *et al.* (2007). Luznik *et al.* (2007) have obtained PIV measurements in the near-bottom unstratified part of a boundary layer on the continental shelf off the coast of South Carolina and Georgia, and examined turbulence spectra and isotropy. Recently, Lozovatsky *et al.* (2008*a, b*) examined the phase variation of the velocity profiles, kinetic energy, dissipation rate as well as peak shear at three locations in the northwestern East China Sea, each having a different barotropic tidal environment.

Compared to oscillatory flows, the effect of stratification in steady wall-bounded flows has received considerable attention. Open channel flow with fixed temperature difference ΔT was studied using DNS by Nagaosa & Saito (1997). Armenio & Sarkar (2002) studied closed channel flow with a fixed temperature difference ΔT across the channel with LES. Applying a fixed temperature difference across the channel leads to a heat flux at the upper and lower boundaries. However, over most of the ocean, the sea floor can be well approximated by an adiabatic boundary condition. This motivated the study of Taylor, Sarkar & Armenio (2005) who performed LES of open channel flow with an adiabatic bottom and constant heat flux at the top surface. More recently, a stratified bottom Ekman layer was studied using LES by Taylor & Sarkar (2007) who focus on the properties of internal gravity waves forced by turbulence and by Taylor & Sarkar (2008) who discuss stratification effects on the boundary layer characteristics. Taylor & Sarkar (2008) propose a buoyancy-related modification of the log-law profile as an alternative to Monin–Obukhov theory (which is inapplicable when the wall buoyancy flux is zero) and show that the modification leads to good agreement between the friction velocity estimated from the profile method and the true value.

After surveying the existing literature, it is clear that the effect of an external stratification on an oscillatory boundary layer has not been the subject of systematic study. While Sakamoto & Akitomo (2009) reported a single simulation with low stratification in the context of a broader study, they did not consider a variety of stratification levels. In contrast, the present study focuses on the effect of stratification on the phase-dependent properties of turbulence and internal waves in a tidal boundary over a range of stratifications, $0 < N_\infty^2/\omega^2 < 2500$. We select $Re_s = 1790$, which has been studied in detail when $N_\infty^2 = 0$ using LES (Salon *et al.* 2007) and laboratory experiments (Jensen *et al.* 1989) and should result in active near-wall turbulence over most of the cycle.

2. Formulation of the problem

The near-bottom flow resulting from a current oscillating with the M_2 tidal period of 12.4 h on a flat bottom is illustrated in figure 1(*a*). The bottom is adiabatic while there is a background thermal stratification with constant buoyancy frequency N_∞. The free-stream velocity,

$$U_{\infty,d}(t_d) = U_{0,d}\,\sin(\omega_d t_d), \tag{2.1}$$

is forced by an imposed pressure gradient,

$$\frac{\mathrm{d}p_d}{\mathrm{d}x_d}(t_d) = -\rho_{0,d}U_{0,d}\omega_d\,\cos(\omega_d t_d). \tag{2.2}$$

Here, subscript d denotes dimensional variables. The phase variation of the free-stream velocity (figure 1*b*) shows that it is antisymmetric, $U_{\infty,d}(-\phi) = -U_{\infty,d}(\phi)$. Furthermore, the flow accelerates during $0 < \phi < \pi/2$ in response to a positive pressure force and decelerates during $\pi/2 < \phi < \pi$ when the pressure force is negative. Owing to the symmetry in the problem, it is sufficient to consider the phase variation of flow statistics during a half-cycle, $0 < \phi < \pi$ that spans 6.2 h; the response in the other half-cycle is either the same or the mirror image. The rotation of earth is neglected in the present work so as to focus on the effect of stratification on the turbulent velocity and thermal boundary layers. The coordinates x, y, z denote streamwise, spanwise (cross-stream) and vertical directions, respectively, while u, v and w are the corresponding velocity components.

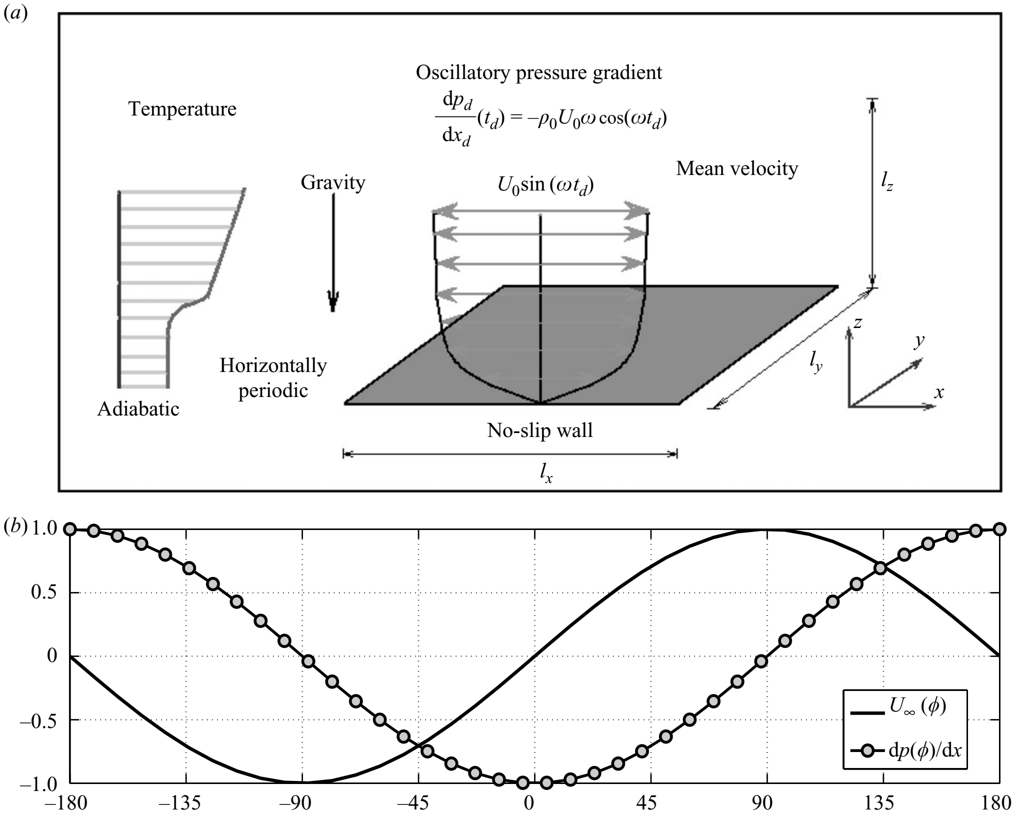

FIGURE 1. (*a*) Schematic of the problem, (*b*) non-dimensional values of imposed pressure gradient and free-stream velocity as a function of tidal phase.

2.1. *Governing equations*

LES is used to obtain the filtered (denoted by overbar) velocity and temperature fields by numerical solution of the Navier–Stokes equations under the Boussinesq approximation, written in dimensional form as

$$\nabla \cdot \overline{\boldsymbol{u}}_d = 0, \tag{2.3a}$$

$$\frac{\partial \overline{\boldsymbol{u}}_d}{\partial t_d} + \overline{\boldsymbol{u}}_d \cdot \nabla \overline{\boldsymbol{u}}_d = -\frac{1}{\rho_{0,d}} \nabla \overline{p'_d} + U_{0,d}\omega_d \cos(\omega_d t_d)\boldsymbol{i} + \nu_d \nabla^2 \overline{\boldsymbol{u}}_d + g_d \beta_d \overline{\theta'_d} \boldsymbol{k} - \nabla \cdot \boldsymbol{\tau}_d, \tag{2.3b}$$

$$\frac{\partial \overline{\theta_d}}{\partial t_d} + \overline{\boldsymbol{u}}_d \cdot \nabla \overline{\theta_d} = \kappa_d \nabla^2 \overline{\theta_d} - \nabla \cdot \boldsymbol{\lambda}_d. \tag{2.3c}$$

Here $\overline{p'_d}$ denotes deviation from the background pressure. The quantities $\boldsymbol{\tau}_d$ and $\boldsymbol{\lambda}_d$ which are the subgrid-scale stress tensor and density flux vector, respectively, require models for closure.

The dimensional quantities in the problem are the free-stream velocity amplitude $U_{0,d}$, tidal frequency ω_d, background temperature gradient $d\theta_d/dz_d|_\infty$, and the dimensional fluid properties: molecular viscosity ν_d, thermal diffusivity κ_d, thermal expansion coefficient β_d and density ρ_d. The variables in the problem are non-dimensionalized as follows:

$$\left.\begin{aligned} t = t_d\omega_d, \quad \boldsymbol{x} = (x, y, z) = \frac{(x_d, y_d, z_d)}{U_{0,d}/\omega_d}, \quad p = \frac{p_d}{\rho_{0,d}U_{0,d}^2}, \\ \boldsymbol{u} = (u, v, w) = \frac{(u_d, v_d, w_d)}{U_{0,d}}, \quad \theta = \frac{\theta_d}{\dfrac{U_{0,d}}{\omega_d}\left.\dfrac{d\theta_d}{dz_d}\right|_\infty}. \end{aligned}\right\} \tag{2.4}$$

The resulting non-dimensional form of the governing equations is

$$\nabla\boldsymbol{\cdot}\overline{\boldsymbol{u}} = 0, \tag{2.5a}$$

$$\frac{\mathrm{D}\overline{\boldsymbol{u}}}{\mathrm{D}t} = -\nabla\overline{p'} + \cos(t)\boldsymbol{i} + \frac{1}{Re}\nabla^2\overline{\boldsymbol{u}} + Ri\overline{\theta'}\boldsymbol{k} - \nabla\boldsymbol{\cdot}\boldsymbol{\tau}, \tag{2.5b}$$

$$\frac{\mathrm{D}\overline{\theta}}{\mathrm{D}t} = \frac{1}{RePr}\nabla^2\overline{\theta} - \nabla\boldsymbol{\cdot}\boldsymbol{\lambda}. \tag{2.5c}$$

The flow is governed by three non-dimensional parameters: the Reynolds number Re, Richardson number Ri and Prandtl number Pr, where

$$Re \equiv \frac{aU_{0,d}}{\nu_d} = \frac{U_{0,d}^2}{\omega_d\nu_d}, \quad Ri \equiv \beta_d g_d \left.\frac{\mathrm{d}\overline{\theta_d}}{\mathrm{d}z_d}\right|_\infty \frac{1}{\omega_d^2} = \frac{N_\infty^2}{\omega_d^2}, \quad Pr \equiv \frac{\nu_d}{\kappa_d}. \tag{2.6}$$

Here, $a = U_{0,d}/\omega_d$ and N_∞ is the background value of buoyancy frequency, assumed constant. The following Reynolds number

$$Re_s = \frac{U\delta_s}{\nu_d} = \sqrt{2Re}, \tag{2.7}$$

based on the Stokes boundary layer thickness, $\delta_S = \sqrt{2\nu_d/\omega_d}$, is a commonly used alternative to Re. We employ Re_s rather than Re_δ to denote the Stokes Reynolds number since, in geophysical boundary layers, the latter expression is often used for definitions involving the friction velocity.

2.2. *Numerical method*

The simulations use a mixed spectral/finite difference algorithm (see Bewley 2007 for details). Derivatives in the horizontal directions are treated with a pseudo-spectral method, the grid is staggered in the vertical, and derivatives in the vertical direction are computed with second-order finite differences. A low-storage third-order Runge–Kutta–Wray method is used for time stepping, and viscous terms are treated implicitly with the Crank–Nicolson method. The eddy viscosity and diffusivity coefficients, ν_T and κ_T defined by (2.8) and (2.9), are computed using current values of velocity and temperature. Then, the subgrid eddy fluxes involving ν_T and κ_T are treated with the Crank–Nicolson method. The code has been parallelized using message passing interface (MPI).

Periodicity is imposed in the horizontal x and y directions. The bottom boundary, $z = 0$, has zero velocity and zero temperature gradient. The top boundary is an artificial boundary corresponding to the truncation of the domain in the vertical direction. Rayleigh damping or a ‘sponge’ layer (see e.g. Klemp & Durran 1983) is used so as to minimize spurious reflections from the artificial boundary into the ‘test’ section of the computational domain. The velocity and scalar fields are relaxed towards the background state in the sponge region by adding damping functions $-\sigma(z)\,[\boldsymbol{u}(\boldsymbol{x}, t) - U_\infty(t)\boldsymbol{i}]$ and $-\sigma(z)\,[\theta(\boldsymbol{x}, t) - \theta_\infty(z)]$ to the right-hand side of the momentum and scalar equations, respectively. Here $\theta_\infty(z) = z\,\mathrm{d}\theta/\mathrm{d}z|_\infty$ is the background temperature profile and $\sigma(z)$ increases exponentially from $\sigma(z = 70\delta_s) = 0$

to $\sigma(z=90\delta_s)=20$. The pressure boundary conditions are $p'=0$ at the bottom wall and $\partial p'/\partial z=0$ at the top of computational domain.

The unstratified, oscillating flow is initialized with the velocity field from fully developed channel flow with a steady $\mathrm{d}p/\mathrm{d}x=-1$ after damping the velocity fluctuations outside of the boundary layer. After at least 15 cycles of the oscillating flow, a linear temperature gradient is applied at $\phi\sim 0°$, this point will be taken to be $t=0$ for the rest of the paper. Variable time stepping with a fixed CFL number of 0.72 is used. The time step varies significantly, from 10^{-4} in the turbulent phase to 10^{-3} in the quasi-laminar phase. One cycle of the passive scalar case took approximately 80 CPU processor hours while the strongly stratified case took 40 CPU processor hours.

2.3. *Subgrid scale model*

The mixed model (Zang, Street & Koseff 1993; Vreman, Geurts & Kuerten 1997) that is used here for the SGS stress tensor, $\boldsymbol{\tau}$, has a scale similarity part and a eddy viscosity part. The SGS heat flux $\boldsymbol{\lambda}$ is obtained using a dynamic eddy diffusivity model (Armenio & Sarkar 2002). The expressions for the SGS models are as follows:

$$\tau_{ij} = -2\nu_T \overline{S_{ij}} + \widehat{\overline{u}_i\overline{u}_j} - \widehat{\overline{u}}_i\widehat{\overline{u}}_j, \qquad \nu_T = C\overline{\Delta}^2|\overline{\boldsymbol{S}}| \tag{2.8}$$

and

$$\lambda_j = -\kappa_T\frac{\partial\overline{\theta}}{\partial x_j}, \qquad \kappa_T = C_\theta\overline{\Delta}^2|\overline{\boldsymbol{S}}|. \tag{2.9}$$

Here, C and C_θ are the Smagorinsky coefficients evaluated through a dynamic procedure introduced by Germano *et al.* (1991). Averaging over horizontal planes is employed to prevent excessive back scattering owing to large local fluctuations. The dynamic procedure involves the introduction of an additional test filter denoted by $\widehat{(\cdot)}$. The model coefficient C in the SGS stress model is given by

$$C = \frac{\langle M_{ij}(L_{ij}-H_{ij})\rangle}{\langle M_{kl}M_{kl}\rangle}, \tag{2.10}$$

where

$$L_{ij} = \widehat{\overline{u}_i\overline{u}_j} - \widehat{\overline{u}}_i\widehat{\overline{u}}_j, \quad M_{ij} = 2\overline{\Delta}^2\widehat{|\overline{\boldsymbol{S}}|\overline{S}_{ij}} - 2\widehat{\overline{\Delta}}^2|\widehat{\overline{\boldsymbol{S}}}|\widehat{\overline{S}}_{ij}, \tag{2.11}$$

$$H_{ij} = \widehat{\overline{\widehat{\overline{u}}_i\widehat{\overline{u}}_j}} - \widehat{\overline{\widehat{\overline{u}}}}_i\widehat{\overline{\widehat{\overline{u}}}}_j - \left(\widehat{\overline{\overline{u}}_i\overline{\overline{u}}_j} - \widehat{\overline{\overline{u}}_j\overline{\overline{u}}_j}\right). \tag{2.12}$$

The model coefficient C_θ in the SGS heat flux model is given by

$$C_\theta = \frac{\langle M_i^\theta L_i^\theta\rangle}{\langle M_j^\theta M_j^\theta\rangle}, \tag{2.13}$$

where

$$L_i^\theta = \widehat{\overline{\theta}\overline{u}_i} - \widehat{\overline{\theta}}\widehat{\overline{u}}_i, \quad M_i^\theta = 2\overline{\Delta}^2\widehat{|\overline{\boldsymbol{S}}|\frac{\partial\overline{\theta}}{\partial x_i}} - 2\widehat{\overline{\Delta}}^2|\widehat{\overline{\boldsymbol{S}}}|\frac{\partial\widehat{\overline{\theta}}}{\partial x_i}. \tag{2.14}$$

The test filter, denoted by $\widehat{(\cdot)}$, and grid filter, denoted by $\overline{(\cdot)}$, are applied over only the horizontal directions using a trapezoidal interpolation rule. For instance, application of the explicit filters to a LES variable $\overline{\Psi}_i$ at node i is given by

$$\widehat{\overline{\Psi}}_i = \frac{1}{4}[\overline{\Psi}_{i-1} + 2\overline{\Psi}_i + \overline{\Psi}_{i+1}], \tag{2.15}$$

$$\overline{\overline{\Psi}}_i = \frac{1}{8}[\overline{\Psi}_{i-1} + 6\overline{\Psi}_i + \overline{\Psi}_{i+1}]. \tag{2.16}$$

Case	Re_s	Ri	Pr	l_x	l_y	l_z	N_x	N_y	N_z
1	1790	0	0.7	$50\delta_s$	$25\delta_s$	$70\delta_s$	64	64	360
2	1790	500	0.7	$50\delta_s$	$25\delta_s$	$70\delta_s$	64	64	360
3	1790	2500	0.7	$50\delta_s$	$25\delta_s$	$70\delta_s$	64	64	360

TABLE 1. Simulation parameters.

The filter width ratio $\widehat{\overline{\Delta}}/\overline{\Delta}$ is taken as $\sqrt{6}$, recommended by Lund (1997) to be the optimal choice for filters evaluated using the trapezoidal rule.

2.4. *Domain resolution and initialization*

The computational domain size in the horizontal directions is $l_x = 50\delta_s$ and $l_y = 25\delta_s$. The vertical domain size is $l_z = 70\delta_s$, significantly larger than the boundary layer thickness ($15\delta_s$ for the unstratified case), so as to allow sufficient vertical space for propagation of internal waves. The sponge region spans $70\delta_s$–$90\delta_s$. The computational grid has $64 \times 64 \times 360$ points in the x, y and z directions, respectively, leading to grid steps of $\Delta x^+ = 60$, $\Delta y^+ = 30$, $\Delta z^+_{min} = 2$ and $\Delta z^+_{max} = 20$ in viscous units ν/u_τ. The resolution is sufficient to resolve the near-wall eddies that carry the Reynolds stress; thus, the present simulation is a resolved LES that does not require an additional near-wall model. The domain size and resolution chosen here is the same as in the C2 case of Salon *et al.* (2007). Since the present simulation has spectral accuracy in the horizontal directions, the larger horizontal grid size, 96×96, of the C4 case needed by the second-order accurate finite difference method of Salon *et al.* (2007) is not required here.

The flow is statistically homogeneous in the horizontal and the x–y plane average is used to compute the time dependent mean, $\langle \mathscr{A} \rangle_{xy}(z, t)$, as follows:

$$\langle \mathscr{A} \rangle_{xy}(z, t) = \frac{1}{l_x l_y} \int_0^{l_x} \int_0^{l_y} \mathscr{A}(x, y, z, t)\, \mathrm{d}x\, \mathrm{d}y. \tag{2.17}$$

The Reynolds average $\langle A \rangle (z, \phi)$, which is a function of the height above the bottom z and the tidal phase ϕ, is calculated by a further ensemble average of the x–y plane averages taken at an interval of π. Thus,

$$\langle \mathscr{A} \rangle(z, \phi) = \frac{1}{\mathscr{N}} \frac{1}{l_x l_y} \sum_{n=1}^{\mathscr{N}} \int_0^{l_x} \int_0^{l_y} \mathscr{A}(x, y, z, \phi + n\pi)\, \mathrm{d}x\, \mathrm{d}y. \tag{2.18}$$

The ensemble average over $\mathscr{N}$ half-cycles, calculated after accounting for a sign change if any, takes advantage of the fact that the flow statistics repeat in either symmetric or antisymmetric fashion after every half-cycle; for example, the mean velocity is antisymmetric, $\langle u \rangle (-\phi, z) = - \langle u \rangle (\phi, z)$. The velocity statistics are obtained by ensemble averaging after at least 15 cycles and over a period of 10, 15 and 15 cycles for cases 1, 2 and 3, respectively, so that the initial transient (spin up to a mixed layer from the initial linear thermal profile) of the thermal field is excluded. The thermal statistics are generally computed using plane averages since the mixed layer grows, albeit at a small rate.

2.5. *Selection of simulated cases*

The physical parameters imposed in our present numerical study are given in table 1. All cases have a Reynolds number, based on the Stokes boundary layer thickness of $Re_s = 1790$, corresponding to the flow studied by Salon *et al.* (2007) and also to test case 8 from the experimental study of Jensen *et al.* (1989). Turbulence is present during most of the cycle at $Re_s = 1790$. This choice also allows us to perform a comparison with the results of Jensen *et al.* (1989) and Salon *et al.* (2007), and thus validate the computational model. The focus of the current study is the assessment of stratification effects on the oscillatory boundary layer and, therefore, Ri is varied between cases from 0 (temperature is a passive scalar in this case) to a high value of $Ri = 2500$. The Prandtl number, $Pr = 0.7$, is kept constant between cases. This choice, lower than the value of $Pr \simeq 5$ for heat transport in water, is motivated by our desire to keep the computational cost manageable; note that the ratio of smallest scale of the thermal field to that of the velocity field is proportional to $Pr^{-1/2}$ when $Pr = O(1)$ or $Pr \gg 1$. At high values of Pr, the thermocline that caps the turbulent mixed layer could be stronger owing to reduced molecular diffusion of temperature and the characteristics of stratified turbulence in that region could be different than the $Pr = 1$ case considered here. The effect of Pr in a stratified bottom boundary layer is deserving of a separate systematic study.

The choice of simulation parameters can be placed in the context of the oceanic bottom boundary layer as follows. Take the viscosity of water to be $\nu = 10^{-6}\,\mathrm{m}^2\,\mathrm{s}^{-1}$, amplitude of current velocity as $U_0 = 1.5\,\mathrm{cm\,s}^{-1}$ and take $\omega = 1.407 \times 10^{-4}\,\mathrm{rad\,s}^{-1}$ corresponding to the M_2 tidal period of 12.4 h. The Stokes boundary layer thickness is $\delta_s = \sqrt{2\nu/\omega} = 0.119\,\mathrm{m}$. The Stokes Reynolds number becomes $Re_s = U_0\delta_s/\nu = 1788$, very close to the value chosen here, while $Re = {Re_s}^2/2 = 1.6 \times 10^6$. The computational domain size of $50\delta_s \times 25\delta_s \times 70\delta_s$ is equivalent to $5.95 \times 2.975 \times 8.925\,\mathrm{m}$. A range for the typical buoyancy time period in the ocean is 1 h–15 min corresponding to $153.7 < Ri < 2460$ for the environmental parameter, $Ri = N_\infty^2/\omega^2$. The choices of Ri in table 1 correspond to a low and a high value in the expected range.

3. Passive scalar case, $Ri = 0$

Results from the $Ri = 0$ case are summarized here with the objective of setting up the context for discussing stratification effects and validating the numerical model by direct comparison with results from the numerical study of Salon *et al.* (2007) and from the laboratory study of Jensen *et al.* (1989) at the same $Re_s = 1790$.

The streamwise velocity $< u^+ > (z^+)$ is plotted in semilog coordinates at an intervals of 30°, along with previous data, in figure 2. The log-law, $u^+ = (1/\kappa)\log(z^+) + B$, applicable to the steady case, is also shown. Here κ is the von Kármán constant taken to be 0.41, and B is the intercept with the u^+ axis taken as 5.2. A log-law is observed between 50°–140°. A significant asymmetry is observed between the accelerating and decelerating phases of the half-cycle, for example, the range of the log-law is larger during the decelerating phase. Figure 2 shows that, over the central span where well-developed turbulence exists, the current result (in grey line) is in excellent agreement with both previous results. In the remaining portion of the cycle, the agreement is still very good especially with respect to the previous laboratory data of Jensen *et al.* (1989).

Figure 3 shows profiles of the streamwise turbulence intensity u_{rms} at several phases. The peak values occur close to the bottom while, at large z, the turbulence dies down to zero (not shown in the figure). The peak value of u_{rms} occurs just past $\phi = 90°$, the point of maximum free-stream velocity. The agreement with previous results is very good throughout the cycle. There is a pronounced outer-layer bulge of the profiles during $120° < \phi < 180°$, similar to experimental observations, that occurs in response

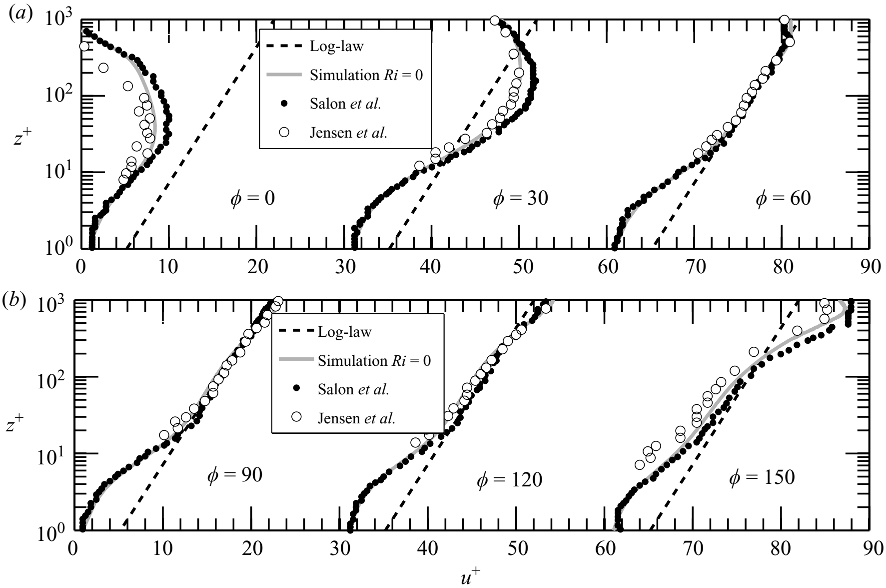

FIGURE 2. Ensemble-averaged profiles of the streamwise velocity in a semilog plot. The present simulation with $Ri = 0$ is shown in a light grey solid line; case C4 of Salon *et al.* (2007) in filled circles; experimental results of Jensen *et al.* (1989) in unfilled circles. The straight dashed line shows the log-law with $\kappa = 0.41$ and $B = 5.2$. (*a*) $\phi = 0°$, 30° and 60°; (*b*) $\phi = 90°$, 120° and 150°. Each profile is staggered by 30 units in the horizontal.

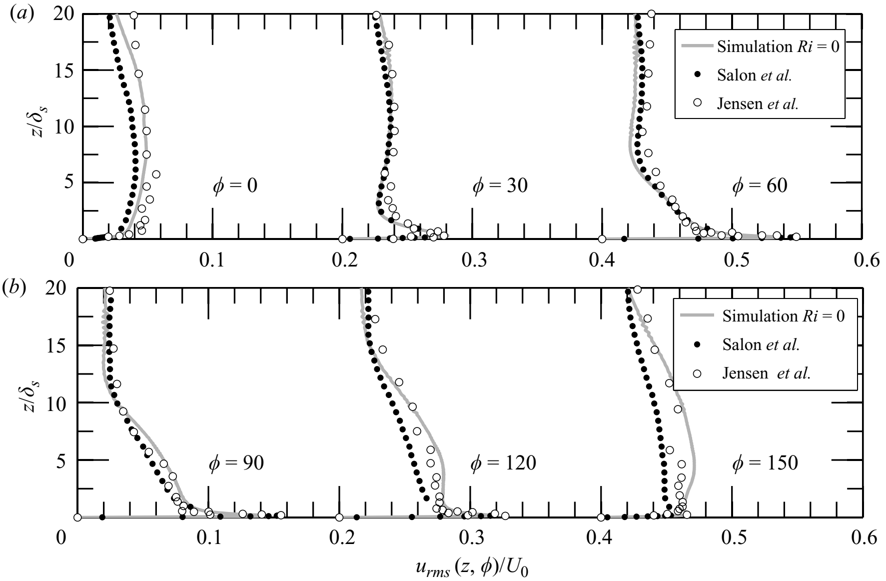

FIGURE 3. Profiles of streamwise turbulence intensity u_{rms} in the passive scalar case. Each profile is staggered by 0.2 units in the horizontal.

to the adverse pressure gradient. Turbulent intensities in the spanwise and vertical directions, which also agree well with data from the previous studies, are not shown here.

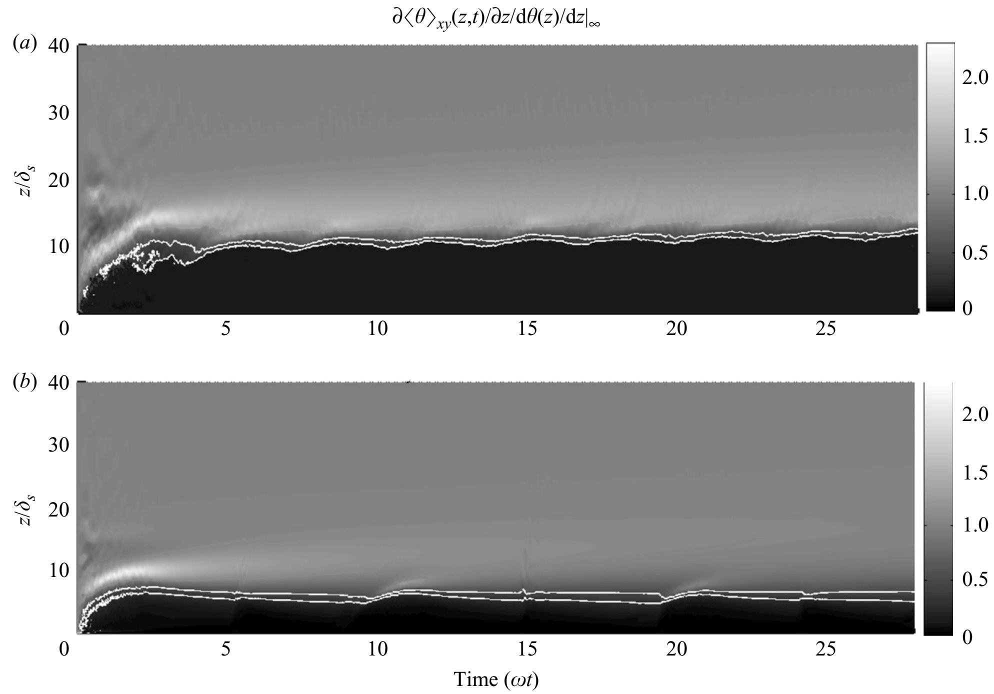

FIGURE 4. Time evolution of vertical profiles of plane-averaged temperature gradient: (*a*) $Ri = 500$ and (*b*) $Ri = 2500$. The lower and upper white lines show contours of $\partial\theta/\partial z = 0.3$ and 0.5, respectively.

4. Overall thermal field

4.1. *Mixed layer growth and entrainment*

The development of the plane-averaged temperature gradient as a function of time is shown in figure 4. The mixed layer (indicated by dark shading) is separated from the outer stratified layer by a thermocline where the temperature gradient changes rapidly exhibiting an overshoot before approaching the background value. Figure 4(*a*) shows that the mixed layer exhibits a small but persistent growth after an initially rapid transient. An interesting phenomenon of periodic modulation of mixed layer growth is also observed, a point that we will return to later. When the stratification level is intensified, the mixed layer height exhibits a substantial decrease as shown by comparison of figures 4(*a*) and 4(*b*).

The mixed layer height h_m is defined by the location where $\partial \langle\theta\rangle_{xy} / \partial z = 0.1$. The gradient Richardson number, defined by

$$Ri_g = \frac{{N_d}^2}{{S_d}^2} = Ri \frac{N^2}{S^2}, \tag{4.1}$$

is often used to demarcate regions of mixing. It is found here that h_m is smaller, by approximately 10 %, relative to the height of the $Ri_g = 0.25$ location. Profiles of the plane-averaged thermal field are shown in figure 5. Figure 5(*b*) illustrates the mixed layer with small temperature gradient as well as a capping thermocline. The unsteadiness of the thermal statistics is clearly shown by comparison of the dashed lines at $t = 15$ with the solid lines at $t = 50$. The mixed layer height, indicated by circles in figure 5, increases with time with the amount of increase strongly inhibited

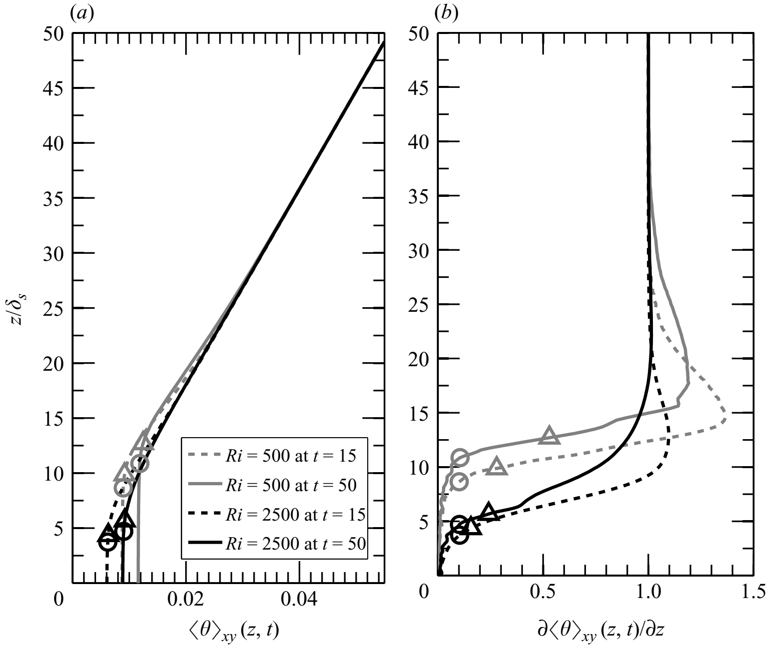

FIGURE 5. Profiles of thermal field: (*a*) temperature and (*b*) temperature gradient. In both plots, lines and symbols in grey correspond to $Ri = 500$ and those in black to $Ri = 2500$. Dashed lines correspond to $t = 15$ and solid lines to $t = 50$. The symbol ○ denotes the location of $\partial \langle\theta\rangle_{xy}(z,t)/\partial z = 0.1$ while the symbol △ locates $Ri_g(z,t) = 0.25$.

in the $Ri = 2500$ case with respect to the $Ri = 500$ case. The thermocline thickens as time goes on and, correspondingly, the overshoot of temperature gradient decreases. Examination of the data shows that both molecular and turbulent diffusion contribute to decreasing the overshoot in the simulation.

4.2. *Behaviour of thermal field over a tidal cycle*

The periodic modulation of the thermal field that occurs over a tidal cycle is examined here. Since the mixed layer height increases continually, plane-averaged quantities are plotted instead of an average over an ensemble with the same phase but different times. Figure 6(*a*) shows that the tidal phase has a strong influence over the mixing of the thermal field and, in particular, the mixed layer height h_m. During most of the deceleration stage, whose extent is from $t = 111.55$ ($\phi = -90°$) to $t = 113.1$ ($\phi = 0°$), the mixed layer height increases. This is linked to an increase of TKE in the *outer* region of the boundary layer during this time span (see figure 6*b*). After reaching its peak value at about $t = 112.82$ (16° before the zero velocity point), the value of h_m decreases consistent with a sharp drop of outer layer TKE. The isotherms at $z \sim 7$–10 show periodic modulation; they are compressed during the decelerating phase when turbulence moves into the outer layer and then relax when the turbulence level plummets towards the end of the deceleration and early acceleration.

The plane-averaged vertical heat flux is shown in figure 6(*c*). The region of intense thermal flux (dark black) is patchy in space/time and occurs in the vicinity of the location of mixed layer height and during the deceleration stage. Interestingly, the upper boundary of this region corresponds to the location of $Ri_g = 0.25$. Finally,

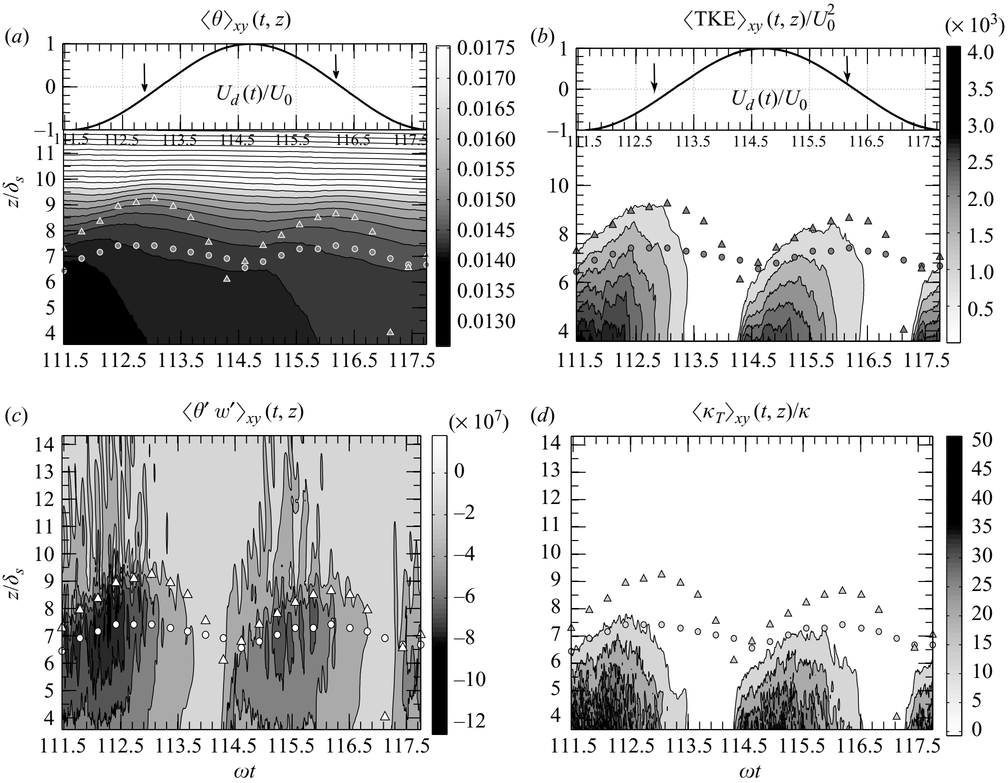

FIGURE 6. Contours, as a function of z and t, in case 3 with $Ri = 2500$ that illustrate the behaviour of the thermal statistics over a half-cycle. The symbol $\circ$ denotes the location of $\partial \langle\theta\rangle_{xy}(z,t)/\partial z = 0.1$ while the symbol $\triangle$ locates $Ri_g(z,t) = 0.25$. The two upper insets shows the background velocity with two downward arrows that show the locations of the local maxima of the mixed layer height h_m. (*a*) Plane-averaged temperature; (*b*) Plane-averaged TKE normalized by U_0^2; (*c*) Plane-averaged vertical heat flux, $\langle\theta' w'\rangle_{xy}(z,t)$ normalized by $U_0^2\, \mathrm{d}\theta/\mathrm{d}z|_\infty/\omega$; (*d*) Eddy diffusivity, $\kappa_T(z,t)$ normalized by molecular diffusivity κ.

the eddy diffusivity κ_T, defined by

$$\kappa_T = -\frac{\langle\theta' w'\rangle_{xy}}{\partial \langle\theta\rangle_{xy}/\partial z}, \tag{4.2}$$

is plotted in figure 6(*d*). Large values of κ_T occur close to the bottom corresponding to the location of large TKE; however, since the fluid is already mixed in that region, the heat flux is not large.

5. Velocity field

Statistics of the velocity field are examined here to investigate the dependence on tidal phase and, in particular, the influence of stratification.

5.1. *Mean velocity*

Vertical profiles of streamwise velocity at different phases are shown in figure 7. During the acceleration stage, the velocity increases rapidly throughout the boundary

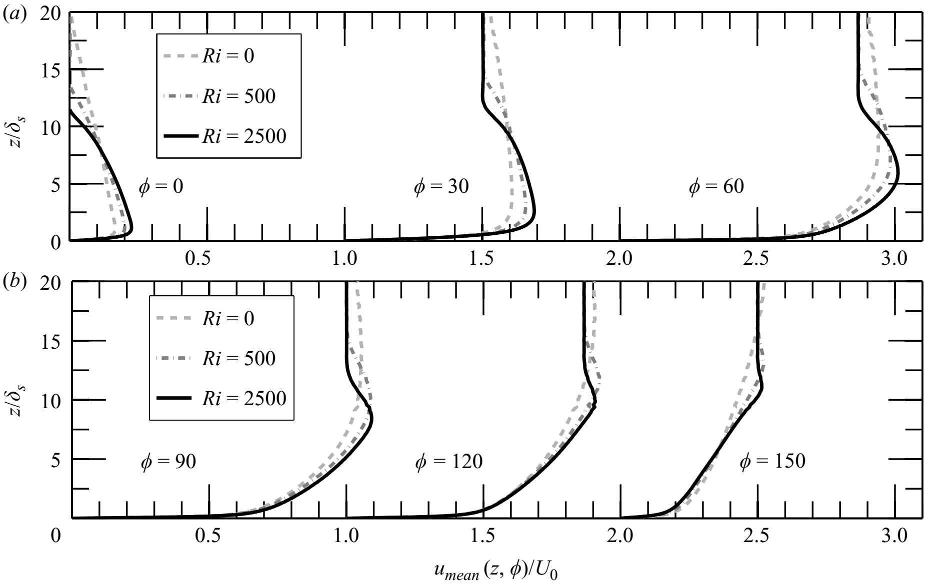

FIGURE 7. Profiles of streamwise velocity at different phases. Case with $Ri = 0$, 500 and 2500 are shown in light grey, dark grey and back lines, respectively. (a) $\phi = 0°$, 30° and 60°; (b) $\phi = 90°$, 120° and 150°. Each profile is staggered by 1.0 unit in the horizontal.

layer, and the profiles become progressively fuller until $\phi = 90°$. Later, during the deceleration stage with adverse pressure gradient, the velocity decreases and the profile become flatter. A phase with zero wall shear stress occurs and, eventually, reverse near-wall flow commences, for instance at $\phi \simeq 175°$ for $Ri = 500$ (although not plotted here, see the bottom panel in figure 20a for a similar example), and a new boundary layer forms in the opposite direction.

The mean velocity exhibits an overshoot with respect to the prevailing free-stream value. The position of maximum overshoot occurs close to the wall at the beginning of the acceleration stage and progressively moves upwards. At $\phi = 90°$, the velocity exceeds unity, the free-stream amplitude. The outer layer 'jet' at $\phi = 90°$ is especially prominent in the $Ri = 2500$ case. The velocity overshoot and its sensitivity to stratification can be explained by the following analysis. Consider the x-momentum equation and integrate it with respect to phase from $\phi = \phi_o$ to $\phi = \phi_t$ to obtain,

$$\left.\begin{aligned} \int_{\phi_0}^{\phi_t} \frac{\partial}{\partial t}\langle U\rangle(z,\phi')\,\mathrm{d}\phi' &= -\int_{\phi_0}^{\phi_t} \langle \mathrm{d}p/\mathrm{d}x\rangle\,(\phi')\,\mathrm{d}\phi' \\ &\quad -\int_{\phi_0}^{\phi_t}\left[\frac{\partial}{\partial z}\langle u'w'\rangle(z,\phi') - \frac{1}{Re}\frac{\partial^2}{\partial z^2}\langle U\rangle(z,\phi')\right]\mathrm{d}\phi', \\ \langle U\rangle(z,\phi_t) - \langle U\rangle(z,\phi_0) &= \langle U\rangle_\infty(\phi_t) - \langle U\rangle_\infty(\phi_0) \\ &\quad -\int_{\phi_0}^{\phi_t}\left[\frac{\partial}{\partial z}\langle u'w'\rangle(z,\phi') - \frac{1}{Re}\frac{\partial^2}{\partial z^2}\langle U\rangle(z,\phi')\right]\mathrm{d}\phi'. \end{aligned}\right\} \quad (5.1)$$

The second line of (5.1) follows from the first after using the relationship, $\langle \mathrm{d}p/\mathrm{d}x\rangle = -\mathrm{d}\langle U\rangle_\infty/\mathrm{d}t$. Denote the velocity overshoot at an arbitrary phase by $\langle \delta U\rangle(z,\phi) = \langle U\rangle(z,\phi) - \langle U\rangle_\infty(\phi)$. Since the streamwise velocity behaves like an odd function of ϕ, it follows that $\langle \delta U\rangle(z,-\phi) = -\langle \delta U\rangle(z,\phi)$ for any given ϕ. Now evaluate (5.1) for $\phi_t = \phi$ and $\phi_0 = -\phi$ and use the relation, $\langle \delta U\rangle(z,-\phi) = -\langle \delta U\rangle(z,\phi)$, to obtain

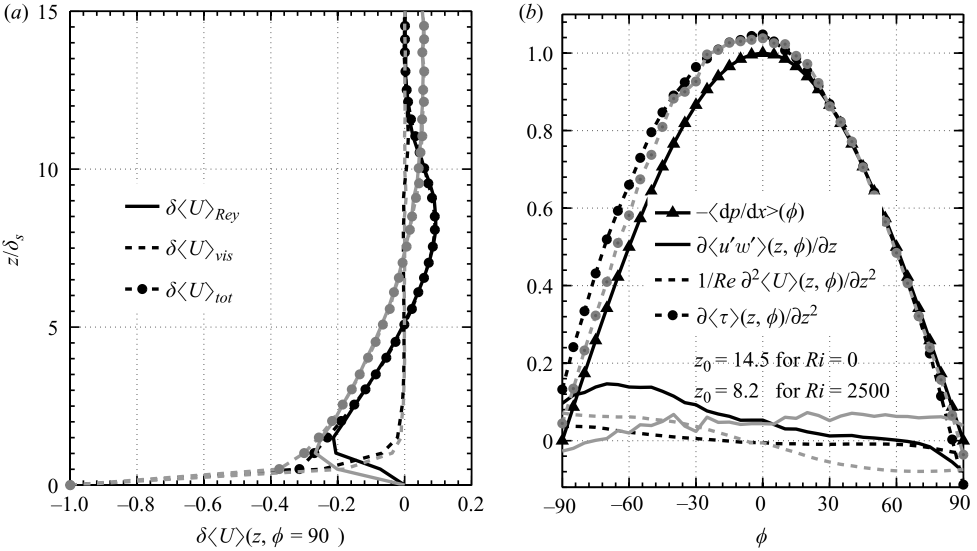

FIGURE 8. Explanation of the velocity overshoot. (*a*) Contribution of Reynolds shear shear stress and viscous shear stress to the overshoot, see (5.2), at $\phi = 90°$ for $Ri = 0$ (shown in light grey shade) and $Ri = 2500$ (black shade), (*b*) variation of various terms in the *x*-momentum equation at a location z_0 as a function of phase.

the following expression for the velocity overshoot:

$$\begin{aligned}\langle \delta U\rangle(z, \phi) &= -\frac{1}{2}\int_{-\phi}^{\phi}\left[\frac{\partial}{\partial z}\langle u'w'\rangle(z, \phi') - \frac{1}{Re}\frac{\partial^2}{\partial z^2}\langle U\rangle(z, \phi')\right] \mathrm{d}\phi', \\ \langle \delta U\rangle(z, \phi) &= \langle \delta U\rangle_{Rey}(z, \phi) + \langle \delta U\rangle_{vis}(z, \phi).\end{aligned} \tag{5.2}$$

Here $\langle \delta U\rangle_{Rey}(z, \phi)$ and $\langle \delta U\rangle_{vis}(z, \phi)$ are velocity overshoots owing to Reynolds shear stress and to viscous stress, respectively.

The overshoot in streamwise velocity profile at $\phi = 90°$ is explained by figure 8(*a*) where $\langle \delta U\rangle_{Rey}$ and $\langle \delta U\rangle_{vis}$, evaluated using their definitions in (5.2), and their sum, $\langle \delta U\rangle_{tot}$, are plotted for cases 1 and 3. The total over shoot $\langle \delta U\rangle_{tot}(z, \phi)$ for both cases is consistent with the overshoot observed in the streamwise velocity at $\phi = 90°$ in figure 7. The maximum overshoot occurs at $z \sim 8.2$ when $Ri = 2500$ while, for the passive case, it occurs higher at $z \sim 14.5$ owing to a thicker turbulent boundary layer. Other than a region very close to the wall, $\langle \delta U\rangle_{vis}$ is negligible compared to $\langle \delta U\rangle_{Rey}$. It is the momentum flux provided by the Reynolds shear stress that, when integrated over the cycle, provides a net positive acceleration to give the overshoot. Furthermore, the gradient of $\langle u'w'\rangle$ is larger in the presence of stratification, leading to a larger overshoot compared to the passive case and the formation of a jet at the top of the boundary layer.

In order to better understand the net positive acceleration provided over a cycle, the different *x*-momentum flux terms are evaluated over the range $-90° \leqslant \phi \leqslant 90°$ and plotted in figure 8(*b*). The evaluations are performed at locations, $z_o = 8.2$ and $z_o = 14.5$, corresponding to cases $Ri = 2500$ and $Ri = 0$, respectively, in order to focus on the location of the maximum overshoot at $\phi = 90°$ for each case. The pressure gradient force (solid line with triangles), responsible for the acceleration of the background velocity, behaves as $\cos(\phi)$. At the wall, it is always balanced by the viscous force; however, since the chosen z_0 are away from the wall, the viscous

Case	Ri	Log-law zone	c_f	Phase lead of τ_w^{max}	$c_{f,avg}$	$(\int \epsilon \, \mathrm{d}z)_{avg}/U_0 u_{\tau,avg}^2$
1	0	40°–140°	0.0043	17°	0.0023	0.2554
2	500	60°–130°	0.0045	23°	0.0024	0.2438
3	2500	80°–125°	0.0048	25°	0.0025	0.2275
Laminar case	–	–	–	45°	–	–

TABLE 2. Comparison of the overall boundary properties between various stratified cases. The subscript *avg* denotes an average over the complete tidal cycle.

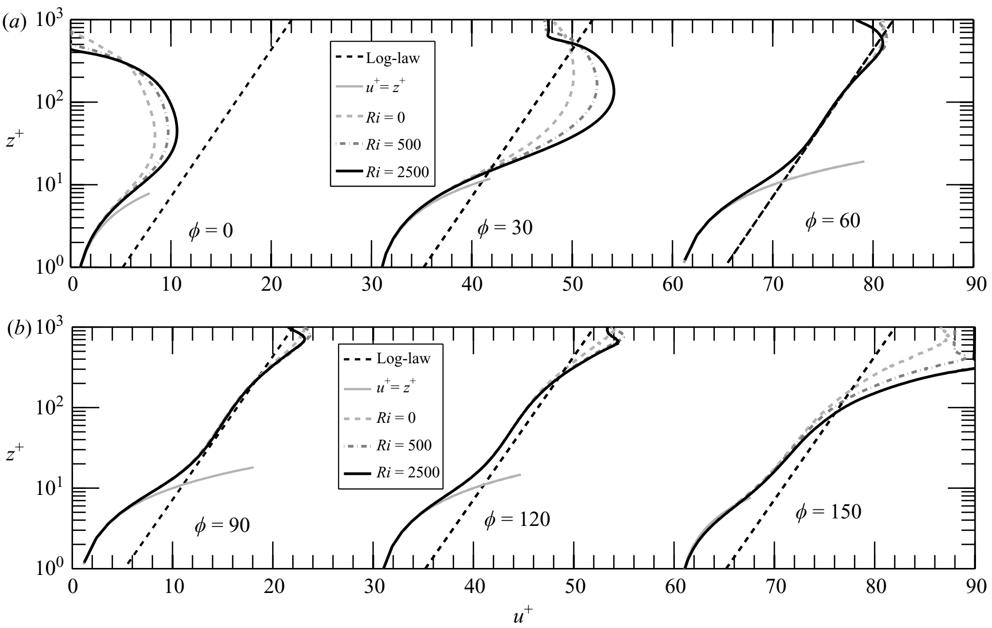

FIGURE 9. Profiles of the streamwise velocity in semilog plot. Each profile is staggered by 30 units in the horizontal.

contribution (dashed lines) is small. The flux due to $\langle u'w' \rangle$ (solid black curve for the $Ri = 2500$ case) is larger than the viscous term in magnitude and it is *strongly positive* during the deceleration stage, almost zero during most of the acceleration stage, and has a short region in the vicinity of $\phi = 90°$ where it is negative. The dashed curve with circles, corresponding to the sum $\partial\langle\tau\rangle(z,\phi)/\partial z$ of all the component fluxes, shows the asymmetry as well as the pronounced positive excess with respect to the pressure gradient which, after integration over the half-cycle, leads to the observed overshoot of mean velocity at $\phi = 90°$.

The effect of stratification on the log-law is shown in figure 9. Although a logarithmic law is present in the stratified cases too, the range of phases where the logarithmic law holds becomes shorter with increasing stratification. Table 2 shows that, during a half-cycle of 180°, the log-law holds for a range of 45° at $Ri = 2500$ instead of 100° as in the passive scalar case. Figure 9 shows that $u^+ = z^+$ in the viscous sublayer ($z^+ < 5$) for all cases. However, there is a noticeable variation

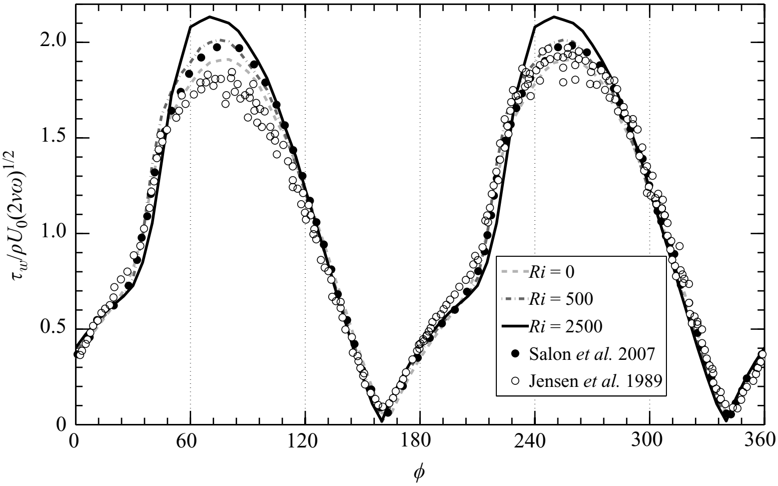

FIGURE 10. Magnitude of wall shear stress τ_w as a function of tidal phase.

of the wall shear stress given by

$$\tau_w = \mu \left[\left(\frac{\partial \langle u \rangle}{\partial z} \right)^2 + \left(\frac{\partial \langle v \rangle}{\partial z} \right)^2 \right]^{1/2}_{z=0} . \tag{5.3}$$

The wall stress leads in phase with respect to free-stream velocity as shown in figure 10. τ_w commences a rapid increase at $\phi \sim 30°$, attains its maximum value before the mean velocity does and, during the decelerating phase, it decreases almost linearly until it becomes zero at $\phi \sim 160°$, signifying commencement of reverse flow. Finally, the wall stress grows slowly along with the development of a new boundary layer in the reverse direction during the late decelerating stage and during the early accelerating phase of the next half-cycle. The maximum value of τ_w leads the maximum value of free-stream velocity by 17° in the passive scalar case. With intensifying stratification, this lead increases to approximately 25° for the case with $Ri = 2500$. The laminar value of the phase lead is 45°. The skin friction coefficient given by

$$c_f = \frac{\tau_{w,max}}{(1/2)\rho U_0^2} \tag{5.4}$$

has been evaluated. The values, listed in table 2, show that there is a small increase in c_f with increasing *Ri*.

5.2. *Turbulent kinetic energy*

TKE contours, shown in figure 11(*a*) for the passive scalar case, show the phase dependence of vertical profiles of TKE. Note that, owing to the problem symmetry, the TKE repeats at a period of 180°. At $\phi = 90°$, the maximum value of TKE occurs very close to the wall. The contours, which slant upwards and to the right after $\phi \sim 90°$, show that the location of maximum TKE in a given vertical profile shifts upwards. The TKE near the bottom decreases during the late deceleration phase, becomes negligible at about 170° (the point of zero mean wall shear stress), and remains small until $\phi = 200°$, equivalently 20°. Nevertheless, during this late deceleration and early acceleration stage, there is significant TKE in the outer layer, associated with residual large-scale turbulence from earlier, that decays slowly. Small-scale turbulence

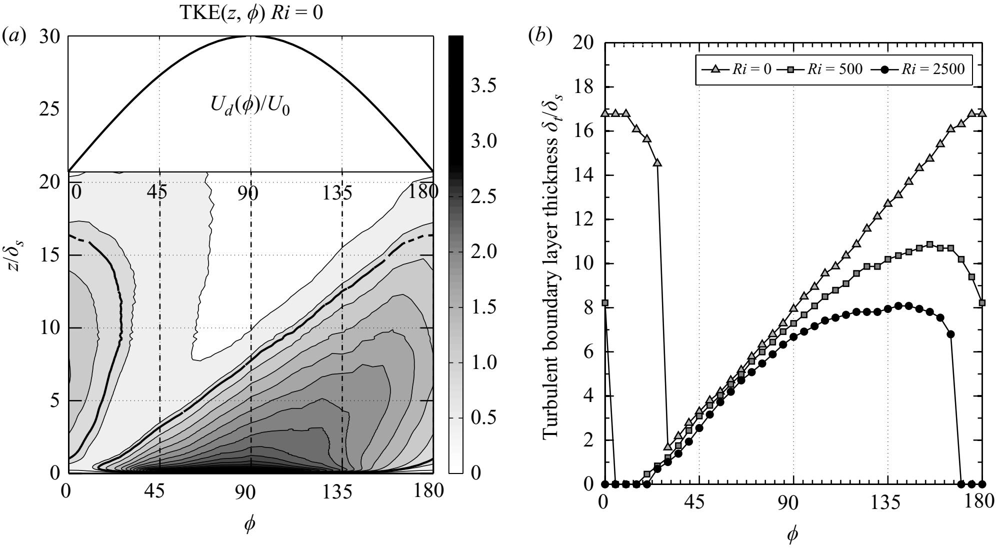

FIGURE 11. (a) Contour plot of the TKE over a half-cycle, normalized by $u^2_{\tau,max}$ for $Ri = 0$. (b) Turbulent layer thickness, based on the TKE isocontour at 10 % of the global maximum value, shown as a function of phase for $Ri = 0$, 500 and 2500.

is generated after approximately 30° when the near-wall shear becomes sufficiently large and a new cycle of turbulence production commences.

The strong variation of mean velocity within a cycle, including an overshoot with respect to the free stream, complicates the definition of a representative boundary layer thickness. One possibility is the definition of a turbulent layer thickness δ_t based on the TKE. The upper boundary of the turbulent layer, defined by the region where the TKE is 10 % of the maximum of its global value, is shown by the dark dotted thick line in figure 11(a). The behaviour of $\delta_t(\phi)$ is compared between cases in figure 11(b). Stratification leads to substantial reduction in the value of δ_t by suppressing the length scale over which turbulence, generated at the wall, can mix momentum. Furthermore, the residual outer-layer turbulence, which occurs during $135^\circ < \phi < (180 + 25)^\circ$ in the passive scalar case, is diminished by stratification, and there is a sudden collapse of large-scale structures once the flow proceeds beyond the stage of turbulence production by near-wall shear. It is worth noting that the maximum value of δ_t occurs during the decelerating stage.

From the preceding discussion it is clear that, during the decelerating stage, there is a strong increase of TKE in the outer layer. To better understand this phenomenon, the *TKE* equation given below is investigated.

$$\frac{\partial k}{\partial t} = P - \epsilon + B - \frac{\partial T}{\partial z}. \tag{5.5}$$

Here k is *TKE* defined by $1/2\,\langle u_i' u_i' \rangle$. The term $\partial T/\partial z$ denotes the transport of the *TKE* containing pressure transport, turbulent transport, viscous transport and SGS transport where

$$T \equiv \frac{1}{\rho_0}\langle p' w' \rangle + \frac{1}{2}\langle u_i' u_i' w' \rangle - \frac{1}{Re}\frac{\partial k}{\partial z} + \langle \tau_{i3}' u_i' \rangle.$$

P is the production term defined as

$$P \equiv -\langle u_i' u_j' \rangle \, \langle S_{ij} \rangle - \langle \tau_{ij} \rangle \langle \overline{S}_{ij} \rangle,$$

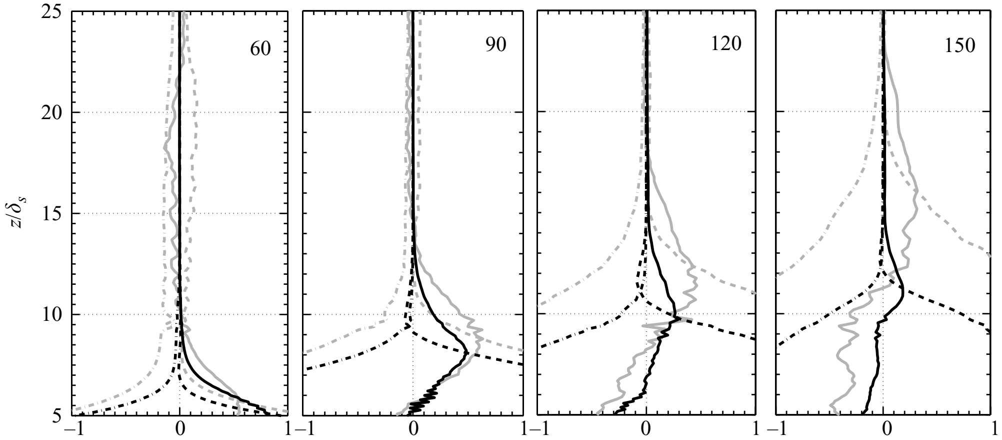

FIGURE 12. Vertical profiles of production (dashed), dissipation (dash-dot) and transport (solid) in the *outer* part of the boundary layer shown for $\phi = 60°, 90°, 120°$ and $150°$, respectively. Light grey and black are used for $Ri = 0$ and 2500, respectively. Here all terms are normalized by $u^4_{\tau,max}/\nu$.

where the last term is the SGS production. The turbulent dissipation rate ϵ is defined as the sum of the resolved and SGS components:

$$\epsilon \equiv \frac{1}{Re}\left\langle \frac{\partial u_i'}{\partial x_j}\frac{\partial u_i'}{\partial x_j}\right\rangle - \left\langle \tau_{ij}\overline{S}_{ij}\right\rangle .$$

Finally, B is the buoyancy flux defined as

$$B \equiv Ri\langle \theta' w'\rangle .$$

The terms in the TKE transport equation are evaluated, and the production, dissipation and transport plotted in figure 12. At $\phi = 60°$, significant values of all three terms are confined to near the wall. In the passive scalar case, the vertical span of all terms extends progressively upwards as ϕ increases to 90° and then to 150°. Thus, the increased outer layer TKE is a consequence of enhanced turbulent transport as well as enhanced shear production in the outer layer as a response to the adverse pressure gradient. At larger z, transport eventually dominates. The $Ri = 2500$ curves in black show that the upward extension of the transport, production and dissipation during the stage of deceleration is substantially less than in the passive scalar case. Nevertheless the shape of the profiles, especially the production and dissipation, are similar between cases.

The overall strength of turbulence can be assessed through a depth-integrated value of TKE where TKE is integrated from $z = 0$ to $z = l_z$ where $l_z = 70\delta_s$ is the height of the computational domain. The behaviour of integrated TKE as a function of phase is shown in figure 13(*a*) and that of integrated production, dissipation and buoyancy flux in figure 13(*b*). The maximum value of $\int TKE\,\mathrm{d}z$ occurs during the deceleration stage at a phase that decreases from $\phi = 135°$ at $Ri = 0$ to $\phi = 100°$ at $Ri = 2500$. Although there is a strong suppression of TKE with increasing Ri as clearly shown in figure 13(*a*), the integrated production and dissipation terms are relatively unaffected since the near-wall turbulence does not feel the overlying stratification. The integrated dissipation and production are negligible during $0° < \phi < 25°$ after which there is a sharp increase owing to the formation of small-scale near-wall turbulence until a peak is attained at approximately $\phi \sim 90°$. Subsequently, during

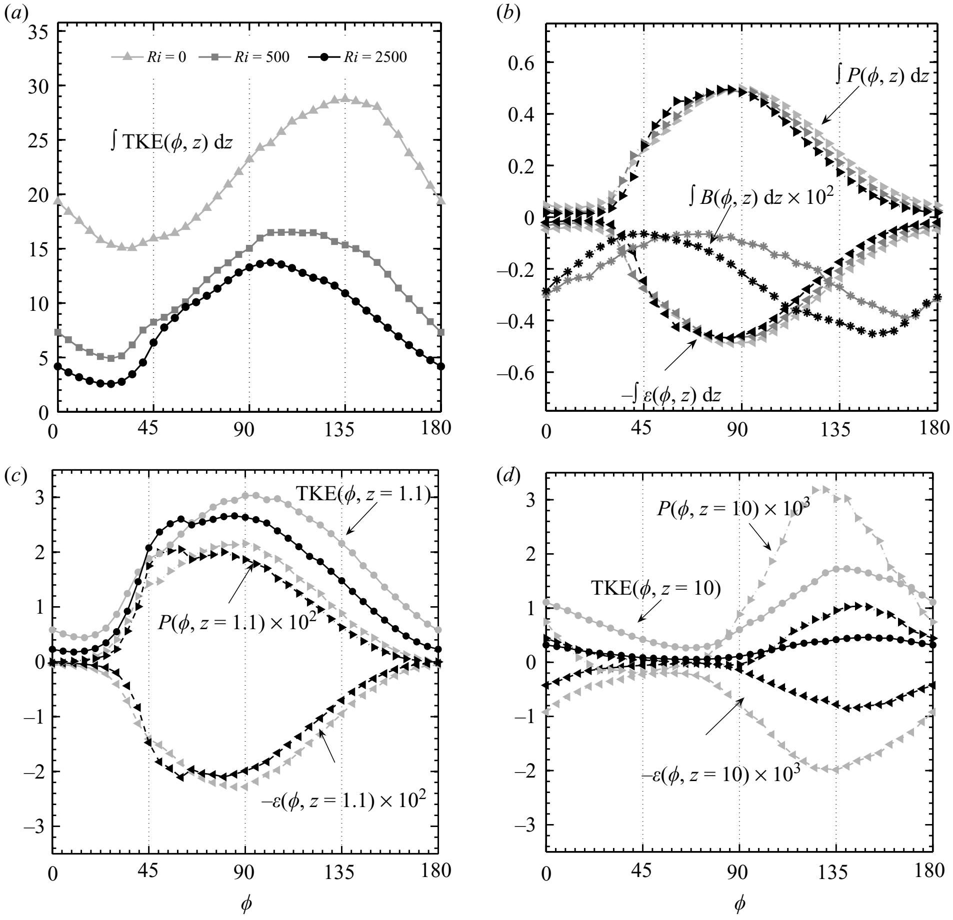

FIGURE 13. (*a*) Integrated (over z) TKE normalized by $u_{\tau,max}^2 \delta_s$ as function of phase. (*b*) Integrated production, integrated dissipation and integrated buoyancy flux over a half tidal cycle. Both are non-dimensionalized by $u_{\tau,max}^2 U_0$. Light grey, dark grey and black are used for $Ri = 0$, 500 and 2500, respectively. (*c*) TKE (normalized by $u_{\tau,max}^2$), production and dissipation as a function of phase at $z = 1.1\delta_s$ for $Ri = 0$ (light grey) and $Ri = 2500$ (black). Both P and ϵ are made non-dimensional by $u_{\tau,max}^4/\nu$. (*d*) Same as in (*c*) for $z = 10\delta_s$.

the deceleration stage, $\int P\,\mathrm{d}z$ and $\int \epsilon\,\mathrm{d}z$ decrease. The depth-integrated buoyancy flux, $\int B\,\mathrm{d}z$, strongly depends on the phase. Although the integrated heat flux is always downwards, its magnitude is large when the integrated production is small, that is, when the mean velocity is small. This observation is consistent with the larger turbulent heat flux and larger mixed layer height during the decelerating phase.

The behaviour of TKE, production and dissipation at a location near the bottom boundary is illustrated by a plot of their phase variation at $z = 1.1\delta_s$ in figure 13(*c*). At this location, *TKE*, P and ϵ attain their peak values at $\phi \sim 90^\circ$ without any phase lag with respect to the maximum of the free-stream velocity. However, in the outer layer ($z = 10\delta_s$), all of these quantities show a significant lag, approximately $\delta\phi \sim 40^\circ$–50°, with respect to the free-stream peak as shown in figure 13(*d*). Thus, the observed phase lag of the peak *TKE* and other related quantities depend on the measurement location from the bottom surface. Such a phase lag has been observed

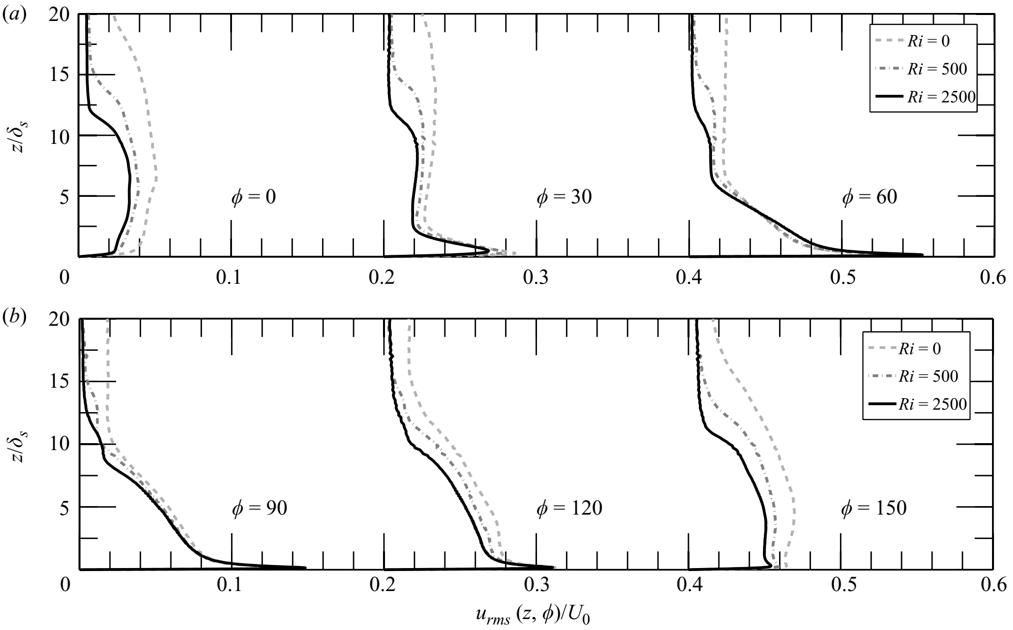

FIGURE 14. Vertical profiles of streamwise turbulence intensity u_{rms}/U_0. Each profile is staggered by 0.2 units in the horizontal.

in the tidal boundary layer. For instance, Burchard *et al.* (1998) show observations of dissipation in the Irish Sea that show a lag of 1 h, equivalently $\delta\phi = 29°$, between dissipation and current at a height 12 m above the seabed. It is worth noting that the phase lag that prevails away from the wall for both P and ϵ does not impact their depth-integrated values, because the regions of large production and dissipation are confined to a small region close to the wall throughout the cycle. On other hand, a significant amount of TKE is transported away from the wall into the outer layer during the decelerating phase (see figure 11*a*) so that the observed outer layer lag gives rise to a corresponding phase lag in the depth-integrated value $\int TKE\,\mathrm{d}z$.

5.3. *Reynolds stresses*

Vertical profiles of Reynolds stresses are discussed in this section. As shown by figure 14, during the fully turbulent phases ($\phi \sim 60°$–$120°$), the streamwise intensities in the near-wall region behave similarly among cases. The maximum value of u_{rms} for $Ri = 2500$ is somewhat greater than the corresponding value in the passive case owing to a somewhat higher wall stress. In the outer layer, where the flow is dominated by buoyancy, u_{rms} is significantly lower in the stratified cases. At $\phi = 150°$ and $\phi = 0°$, phases with low wall stress, the maximum value u_{rms} for all cases occurs away from the bottom wall.

The vertical turbulent intensity, w_{rms}, is shown as a function of phase and height in figure 15. The suppressing effect of buoyancy in the outer region is also present in the w_{rms} profiles and in the profiles of spanwise turbulence intensity (not shown here).

Figure 16 shows profiles of the Reynolds shear stress $\langle u'w'\rangle(\phi, z)/U_0^2$ at various phases during the tidal cycle. At $\phi = 90°$, the maximum value of $\langle u'w'\rangle/U_0^2$ occurs close to the wall with the value for the stratified cases slightly larger than in the passive scalar case. In the outer layer, $\langle u'w'\rangle/U_0^2$ decreases more rapidly in the stratified cases compared to the passive scalar case. During the late deceleration

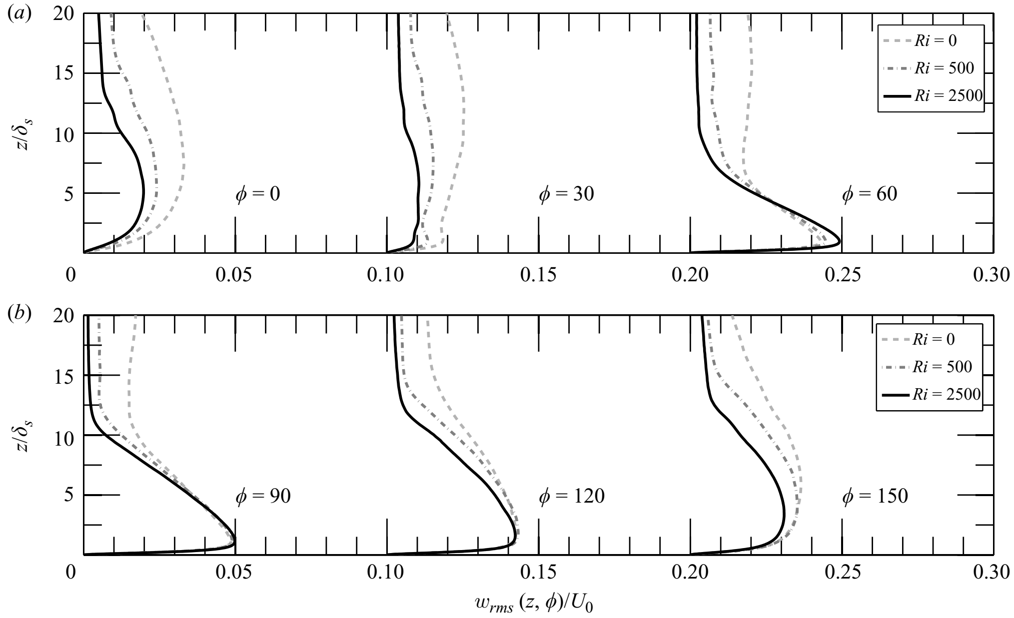

FIGURE 15. Vertical profiles of vertical turbulence intensity w_{rms}/U_0. Each profile is staggered by 0.1 units in the horizontal.

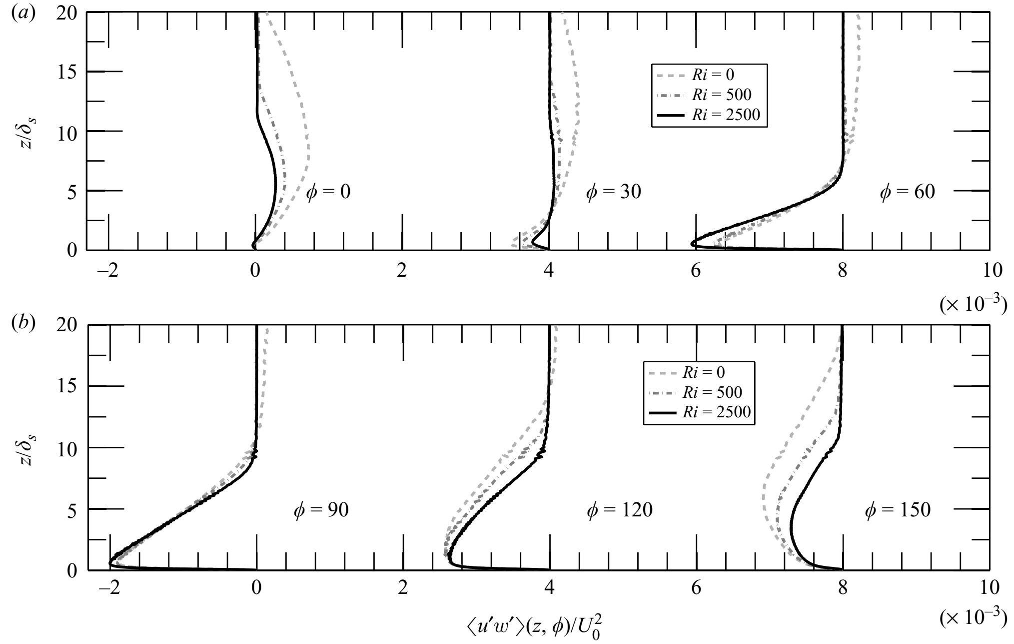

FIGURE 16. Vertical profiles of Reynolds shear stress $\langle u'w' \rangle / U^2{}_0$. Each profile is staggered by 4×10^{-3} units in the horizontal.

stage, there is significant Reynolds shear stress away from the wall owing to large-scale turbulent structures. During the early acceleration stage, $0^\circ < \phi < 30^\circ$, the Reynolds shear stress away from the wall decreases associated with the collapse of these large-scale structures while that near the wall increases as a consequence of progressively increasing near-wall shear.

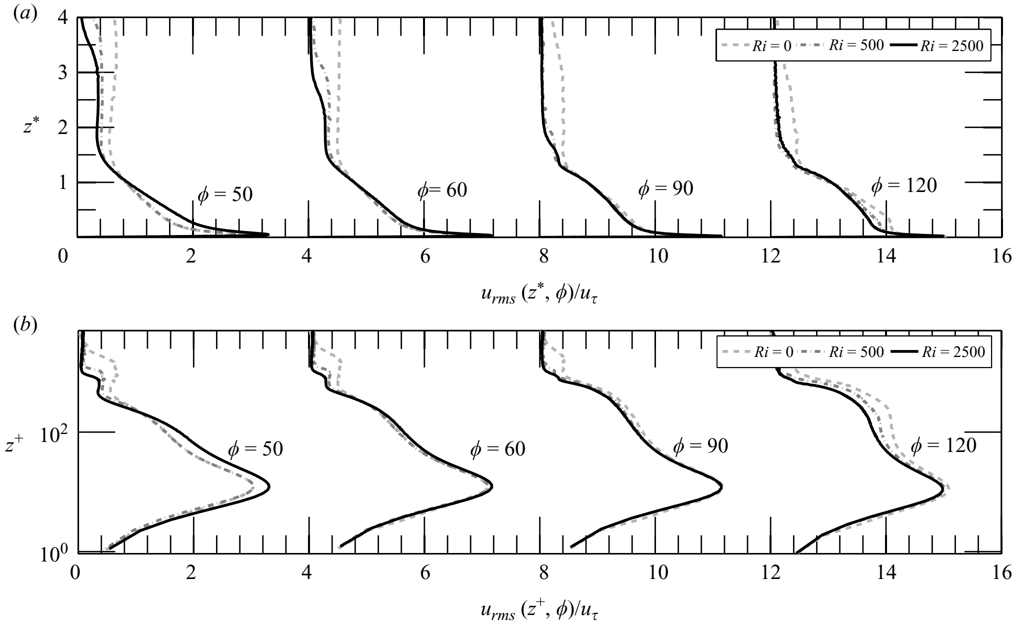

FIGURE 17. (*a*) Profiles of streamwise r.m.s. turbulence normalized by friction velocity u_τ as a function of z^* (z/δ_t) at $\phi = 60°$, $75°$, $90°$ and $105°$. (*b*) Profiles replotted using the z^+ coordinate and semilog axes. Each profile is staggered by 4.0 units in the horizontal.

5.4. *Scaling of turbulence profiles*

In figure 17(*a*), we have replotted the streamwise turbulent intensity in the fully turbulent phases using a different normalization: the turbulent boundary layer thickness $\delta_t(\phi)$ for the vertical coordinate and the friction velocity $u_\tau(\phi)$ for u_{rms}. The profiles tend to collapse between the two stratified cases. The $Ri = 0$ profile agrees well with the other two cases for $z/\delta_t < 1$; however there is some difference at larger values of height over the bottom. This normalization cannot be used during the less energetic phases since δ_t and u_τ become very small and may drop to zero during these phases. The applicability of inner layer scaling is assessed in figure 17(*b*). In the viscous sublayer and the buffer layer that span $z^+ < 20$, the profiles are almost indistinguishable between cases. When z^+ is not too large, the differences between cases is small during the acceleration stage and increases somewhat during deceleration. Production, dissipation rate and transport, the three leading terms in the TKE equation, given in (5.5), are plotted in figure 18 as a function of $z^* = z/\delta_t$ for different phases. The normalization factor is u_τ^4/ν, customary for wall-bounded flows. Importantly, the use of δ_t as the appropriate length scale enables good collapse of the profiles among all Ri cases over a wide range of phases $\phi \sim 55°$–$110°$ when the turbulence is energetic. The viscous dissipation rate peaks at the wall where it is balanced by viscous transport, $1/Re\left(\partial^2 k/\partial z^2\right)$. Production reaches it maximum value within the buffer layer, a location where the transport term is negative signifying that it is a sink transporting *TKE* away to other locations. At the edge of the boundary layer where production and dissipation are negligible, the buoyancy flux and the vertical energy flux, $\langle p'w' \rangle$ due to internal wave activity, become important in the stratified cases as will be shown later. In the region with significant turbulence, the balance is, for the most part, between production and dissipation. Since u_τ and

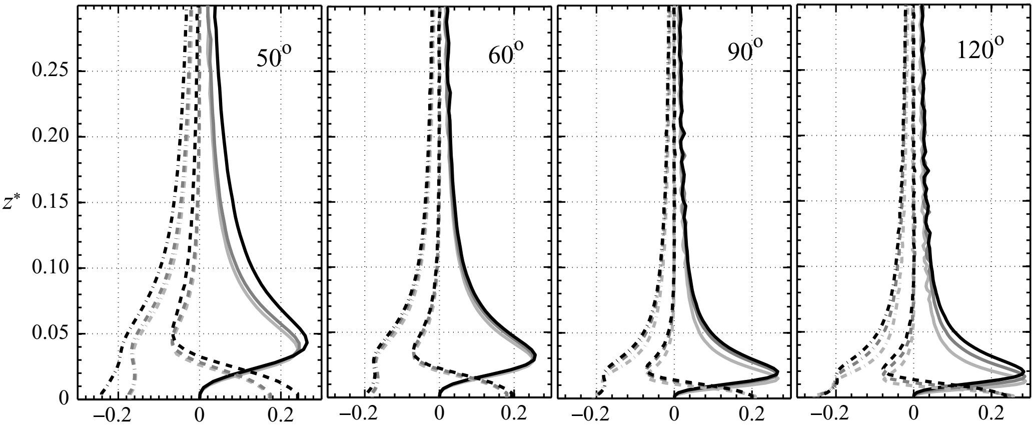

FIGURE 18. Four panels show the profiles of production (solid line), dissipation (dash-dot line) and modified transport (dotted line) normalized by $u_\tau^4(\phi)/\nu$ as function of $z^*(z/\delta_t)$ at $\phi = 50°, 60°, 90°$ and $120°$, respectively. We have used light grey, dark grey and black for $Ri = 0$, 500 and 2500, respectively.

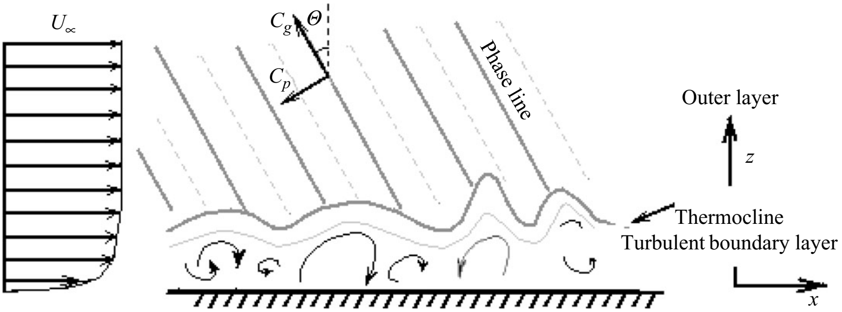

FIGURE 19. Cartoon of internal wave generation from the thermocline excited by turbulent boundary layer. Here C_g and C_p are the group and the phase velocity, respectively.

δ_t become very small during the less energetic phases, this normalization cannot be used for those phases.

6. Internal waves

Flow instabilities and turbulence in the bottom boundary layer can lead to internal gravity waves that propagate in the overlying stratified fluid. For the boundary layer under a steady free-stream (Taylor & Sarkar 2008) internal waves are generated by vertical modulation of the thermocline by a broad spectrum of eddies in the boundary layer. The lines of constant phase are inclined towards the direction of the source velocity relative to the free-stream velocity, similar to waves generated by flow over corrugated surfaces like hills and mountains (Lighthill 1990). Figure 19 provides a schematic of internal gravity waves in a steady current. The group velocity c_g, relative to the free stream, is aligned with the phase line, is orthogonal to the wavenumber vector, and transfers energy upwards from the boundary layer to the background.

The source of internal waves is the turbulent flow in the mixed layer that consists of a broad range of scales. The inclination of the phase line of the internal wave radiated by an eddy depends on the flow induced by the eddy, the mean velocity at the source location, and the free stream velocity and the combination of all those

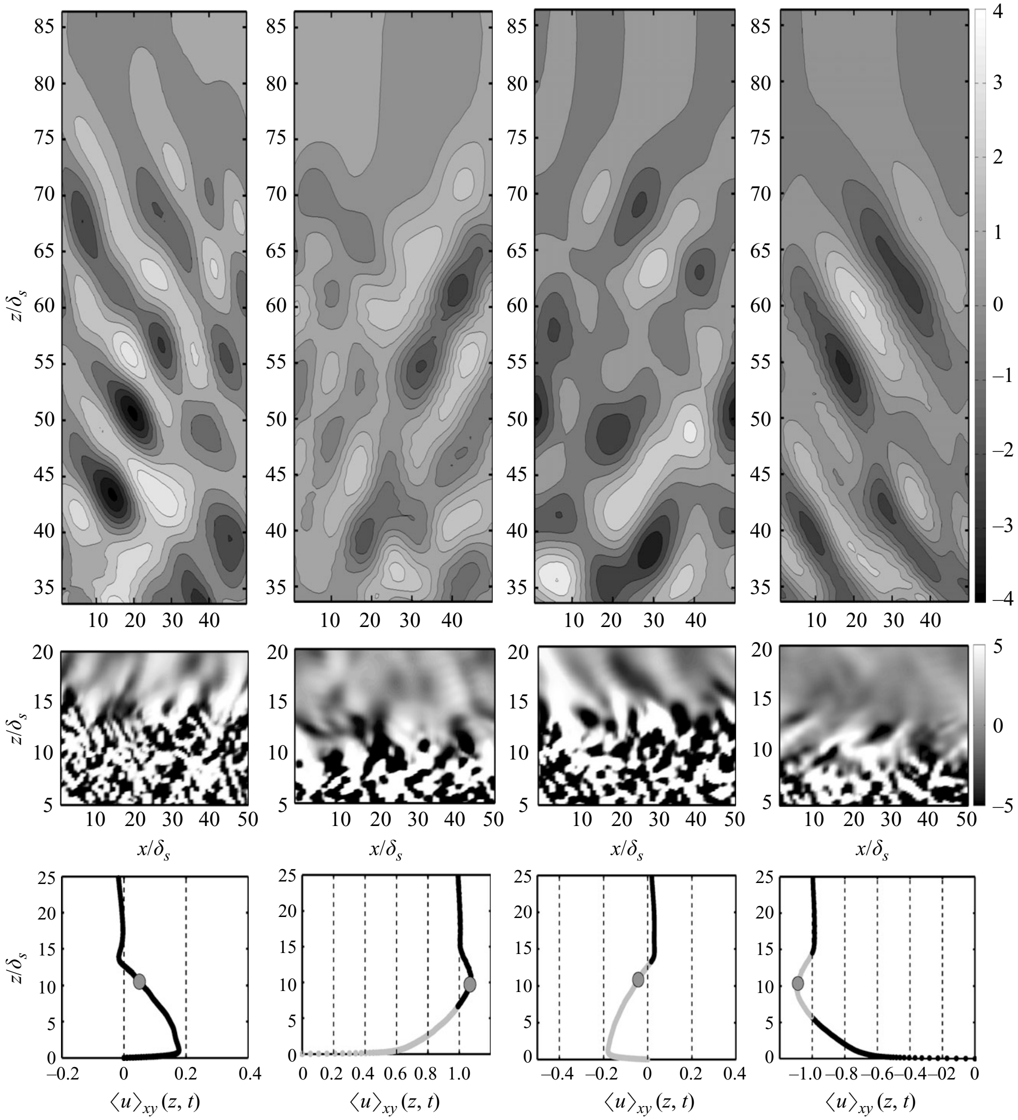

(*a*) (*b*) (*c*) (*d*)

FIGURE 20. Slice of $\partial w'/\partial z$ in the x–z plane for the case with $Ri = 500$ at different tidal phases: (*a*) $\phi = -5°$, (*b*) $\phi = 90°$, (*c*) $\phi = 180°$ and (*d*) $\phi = -90°$. Each part is divided into three panels: top panel shows the waves in the far-field, $z = 35-86$; middle panel shows the turbulent source and near-field waves; bottom panel shows the streamwise velocity profile with black and light grey indicating positive and negative signs of the velocity relative to the free steam. The ○ symbols on the velocity profiles show the location of $\partial\theta(z, t)/\partial z = 0.1$ to demarcate the mixed layer.

phase lines gives rise to the observed wave pattern. For the steady case, the velocities at the internal wave source with respect to free-stream current have mostly the same sign whose value determines the tilt of the phase lines with respect to the vertical: the tilt is forward when the sign of the relative velocity is positive and backward when the sign is negative. In the oscillating flow considered here, the direction of the source velocity with respect to the free stream is phase dependent leading to a more complex wave pattern. This is illustrated by figure 20(*a*–*d*) that shows x–z slices of the $\partial w'/\partial z$

field in a frame moving with free-stream velocity at four different phases of the tidal cycle. The upper panels in the figure show the far-field waves while the middle panel shows turbulence as well as the near-field waves adjacent to the generation region. Clearly, the slope of the phase lines depends on tidal phase and the slope differs between far- and near-fields. The bottom panel, which shows mean velocity profiles at the corresponding times with black showing values positive with respect to the free stream and grey showing negative values, helps to explain the observed phase lines. Although, it is difficult to exactly demarcate the wave source, the generation region is bounded from above by the location of $\partial\theta(z,t)/\partial z = 0.1$, the top of the mixed layer. The snap in figure 20(*a*) corresponds to a late decelerating phase ($\phi \sim -5^\circ$) where a new boundary layer with reverse flow in the bottom relative to the free stream has been formed. The flow velocity, relative to the free stream, is positive in the source region as shown in the bottom panel of figure 20(*a*) leading to phase lines inclined to the front as shown in the middle panel of figure 20(*a*). These forward-inclined waves do not have enough time to propagate into the outer region and the backward-inclined phase lines in the outer region, shown in the upper panel of figure 20(*a*), correspond to internal waves generated during the early accelerating stage of the previous cycle, for example, those in the middle panel of figure 20(*c*–d). When the flow progresses in time, a near-bottom region of negative velocity with respect to the free stream, similar to the conventional steady boundary layer, progressively develops. Figure 20(*b*) shows $\phi = 90^\circ$ where, as shown by the middle panel, waves are generated from the source with no preferred inclination of the phase lines, see middle panel, but the outer region shown in the top panel exhibits forward-inclined waves that were generated previously, for example at $\phi = -5^\circ$ shown in figure 20(*a*). Now, examination of the velocity profile at $\phi = 90^\circ$ reveals that most of the mixed layer has negative relative velocity compared to a small portion with positive relative velocity. Therefore, one would expect generation of backward waves from the source region and, indeed, such phase lines were observed in the steady stratified Ekman boundary layer by Taylor & Sarkar (2007) where the streamwise velocity profile has a shape similar to that seen here at $\phi = 90^\circ$. However, the history of the mean flow is important in the oscillating case; forward phase lines emitted by the predominantly positive velocity at an earlier nearby phase remain adjacent to the boundary layer at $\phi = 0^\circ$ if $c_{g,z}$ is sufficiently small and, consequently, both forward and backward phase lines are observed in the middle panel of figure 20(*b*). Thus, owing to history effects, arriving at a conclusion based on steady currents that, at $\phi = 90^\circ$ in the present oscillating flow, the phase lines would tilt backward is clearly erroneous. During the following deceleration stage, the source is dominated by fluid with negative relative velocity giving rise to waves with phase lines inclined towards the back (middle panel of figure 20*c*) while the outer region still has the forward phase lines of internal waves generated in the previous acceleration stage. In figure 20(*d*), the phase of -90° corresponding to negative free-stream velocity is shown. Here, similar to the phase of 90° shown in figure 20(*b*), there is no clear direction of phase lines adjacent to the boundary layer. However, the phase lines in the far field tilt backward.

The generation of internal gravity waves from the source over a tidal cycle is shown more elaborately in figure 21 through a sequence of nine snaps of the vertical strain field. The corresponding streamwise velocity profile plotted in two different colours (discussed before) is shown above each snap. The sequence begins with figure 21(*a*), corresponding to $\phi = -90^\circ$, and ends at figure 21(*i*), a time corresponding to approximately the same phase as in figure 21(*a*). In figure 21(*a*–*b*), the wave source has both positive and negative values of relative velocity and therefore the phase

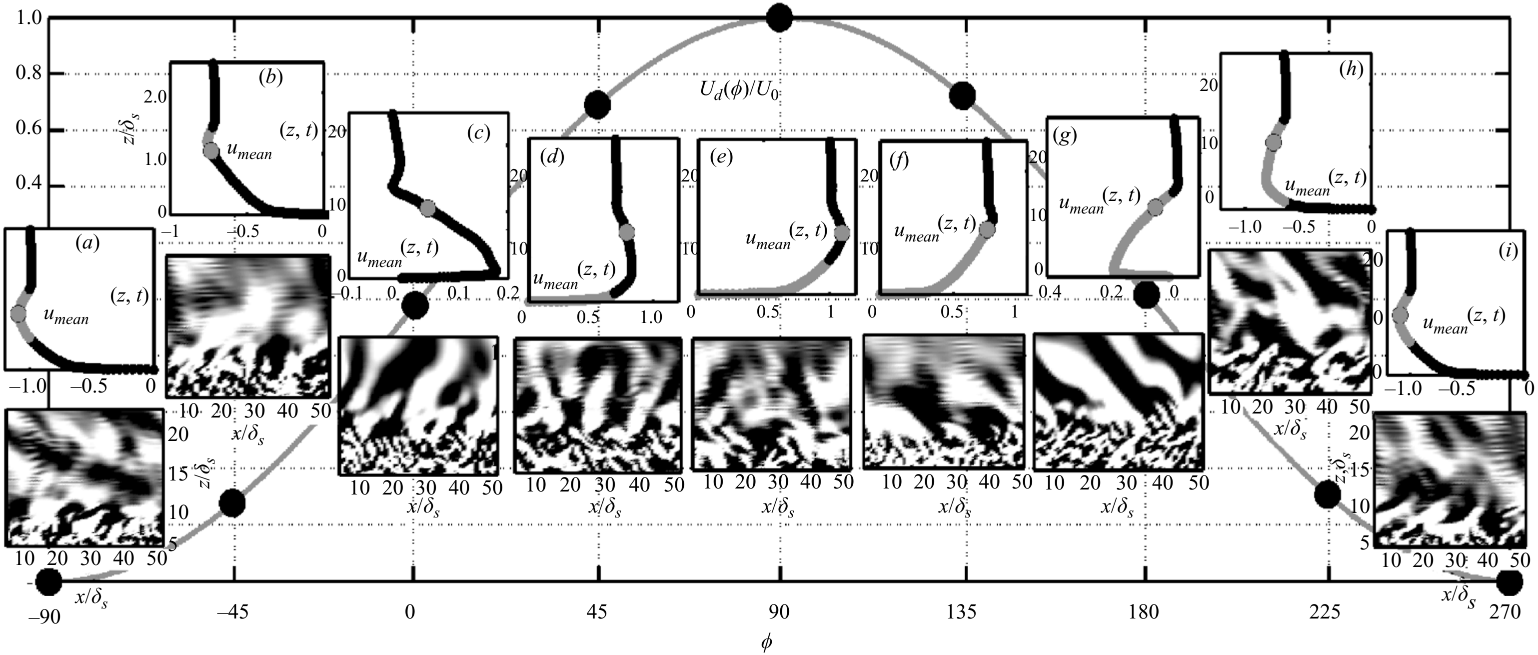

FIGURE 21. In (a)–(i), slices of $\partial w'/\partial z$ in the x–z plane along with streamwise velocity profiles are shown over a time period that spans an entire tidal cycle, shown in the background of the figure. Each slice ($x = 0 - 50$ and $z = 5 - 25$) shows the generation region and near field. In the velocity profile, ○ give the location of $\partial\theta(z, t)/\partial z = 0.1$. Black and light grey portions of the velocity profiles indicate positive and negative sign of the local velocity with respect to free steam velocity, respectively.

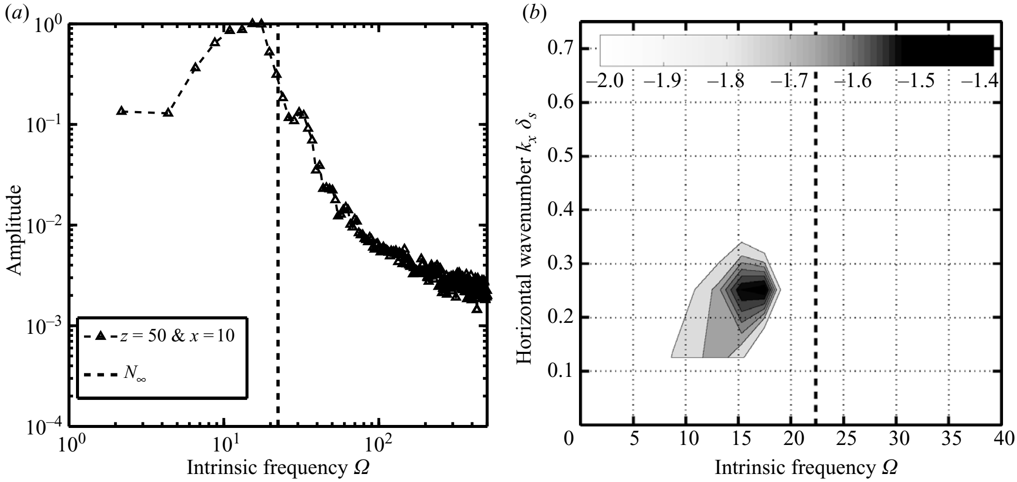

FIGURE 22. (a)Power spectra of the $\partial w'/\partial z(t)$ field (log-scale) as a function of frequency in the case with $Ri = 500$. The time series is taken in a frame moving with free-stream velocity at $z = 50$ and $x = 10$ over a a time span $40.95 < t < 43.9$ which corresponds to $-175° < \phi < -5°$, and the resulting spectra at different spanwise locations are averaged. The dotted vertical line indicates N_∞. (b) The two-dimensional power spectrum (log-scale) of $\partial w'/\partial z(x, t)$ at $z = 50$ plotted as a function of the streamwise wavenumber and intrinsic frequency space. Spanwise averaging is used again. Here, the wavenumber has been normalized with δ_s.

lines have no directional preference. In figure 21(c–d), the wave source is dominated by positive relative velocity and, consequently, generates waves inclined towards the front. At $\phi = 90°$, there is an overshoot of velocity and formation of a jet as discussed previously, leading to a small region of positive relative velocity in addition to the negative velocity of near-bottom fluid. Therefore, both backward and forward phase lines are generated from the source in figure 21(e) due to combined effect of the relative velocity condition during the current phase and previous nearby phases. In figure 21(f), phase lines start bending towards the back and stay backwards at the phases shown in figures 21(g) and 21(h). During the remainder of the acceleration stage, the fluid region very close to wall is retarded and has slower speed than the free stream but the outer layer develops an overshoot in speed leading to figure 21(i), similar to the situation back in figure 21(a), where there are phase lines of both tilts.

In order to quantify the properties of the internal wave field, we have performed a power spectrum analysis of the $\partial w'/\partial z$ field. Unless otherwise mentioned, the $\partial w'/dz$ field is taken in a frame moving with the free-stream velocity. Figure 22(a–b) show one and two-dimensional power spectra, respectively, for the $Ri = 500$ case. The intrinsic frequency or frequency in a frame moving with the free-stream velocity U_∞ is defined as

$$\Omega = \omega_{app} - \boldsymbol{U}\cdot\boldsymbol{k}, \tag{6.1}$$

where $\boldsymbol{k} = (\boldsymbol{k}_x, \boldsymbol{k}_y)$ is the horizontal wavenumber vector and ω_{app} is the apparent frequency in the fixed frame. The time span of the analysed data is taken to be $40.95 < t < 43.9$, a range over which phase lines in the outer layer have a backward tilt. Turbulence generated internal waves are characterized by broadband spectra in both wavenumber and frequency. But eventually, in the far-field the internal waves occupy a narrow band of frequencies as shown in figure 22(a). This frequency range corresponds to phase lines whose angle with the vertical span $40° < \Theta < 62°$. Similar narrow-band internal wave propagation has been observed in laboratory experiments by Sutherland & Linden (1998) and Dohan & Sutherland (2003, 2005).

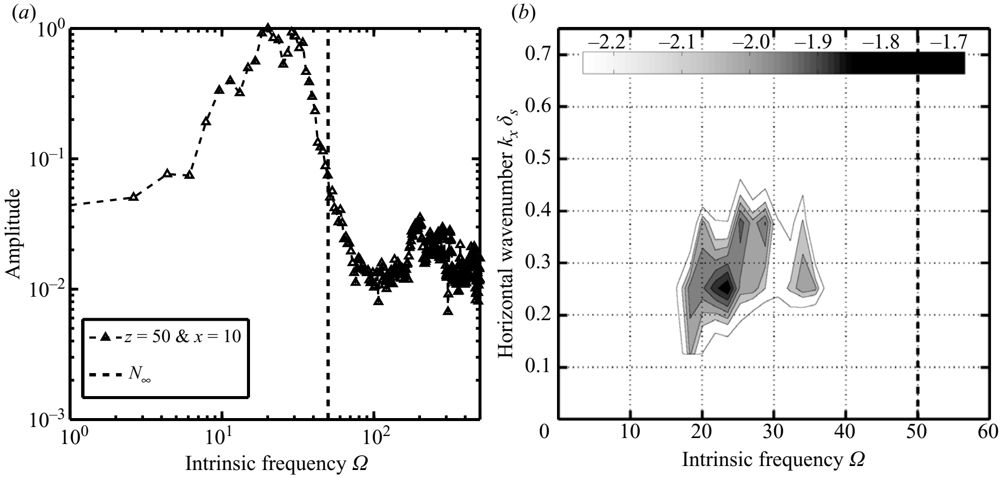

FIGURE 23. Same as figure 22 for $Ri = 2500$.

More recently, Taylor & Sarkar (2008) in their numerical study have also observed a similar narrow band of angles for the steady Ekman bottom boundary layer and have offered a frequency-selective viscous decay model to explain this phenomenon. Similar results are obtained for the strongly stratified case as shown in figure 23.

The relative importance of the energy flux $\langle p'w'\rangle$ carried by the internal waves at a particular level, say $z = z'$, with respect to the other energy fluxes can be obtained by integrating the TKE equation up to height z' and measuring the terms in the resulting equation (6.2). Here z' is taken to be sufficiently larger than the boundary layer height δ_t so that viscous and turbulent transport are negligible:

$$\frac{\int_0^z P(z',\phi)\,\mathrm{d}z'}{\langle p'w'\rangle(z,\phi)} - \frac{\int_0^z \epsilon(z',\phi)\,\mathrm{d}z'}{\langle p'w'\rangle(z,\phi)} + \frac{Ri\int_0^z \langle\theta'w'\rangle(z',\phi)\,\mathrm{d}z'}{\langle p'w'\rangle(z,\phi)} = 0. \tag{6.2}$$

The inverse of the three terms of (6.2) quantifies the internal wave energy flux relative to the integrated dissipation, production and buoyancy flux, respectively. These quantities are shown for $Ri = 500$ and 2500 at $\phi = 90°$ in figure 24. For both cases, the vertical energy flux is less than 1 % compared to the integrated dissipation and production indicating that the internal waves have negligible direct effect on the boundary layer turbulence. However, as shown by figure 24(*c*), the integrated buoyancy flux and the vertical energy flux are comparable suggesting that the energy carried away by internal waves that could then potentially cause non-local mixing (for more complicated background conditions than the one considered here) is comparable to the local mixing of density. The average vertical energy flux, defined by

$$\langle p'w'\rangle_{avg}(\phi) = \frac{1}{l_z - h_m}\int_{h_m}^{l_z} \langle p'w'\rangle(z',\phi)\,\mathrm{d}z', \tag{6.3}$$

where h_m is the height of the mixed layer as defined previously, also varies over the phase as shown in figure 25. The average vertical energy flux peaks during the laminar phase ($\phi \sim 0°$) of the cycle because of the buildup of internal waves generated during the previous turbulent portion of the cycle. According to the profile of $\langle p'w'\rangle/Ri\int_0^z\langle\theta'w'\rangle\,\mathrm{d}z'$ at $\phi \sim 0°$ (not shown here), its value is somewhat larger in the outer region, approximately 0.3 compared to 0.2 at $\phi = 90°$.

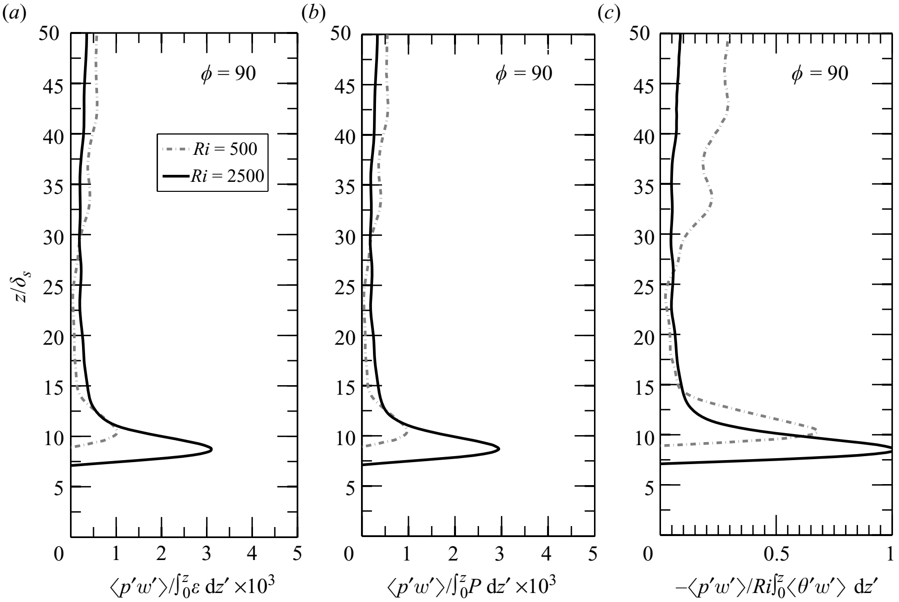

FIGURE 24. Vertical energy flux normalized by (*a*) the integrated turbulent dissipation, (*b*) the integrated production and (*c*) the integrated buoyancy flux at $\phi = 90$ for $Ri = 500$ and 2500.

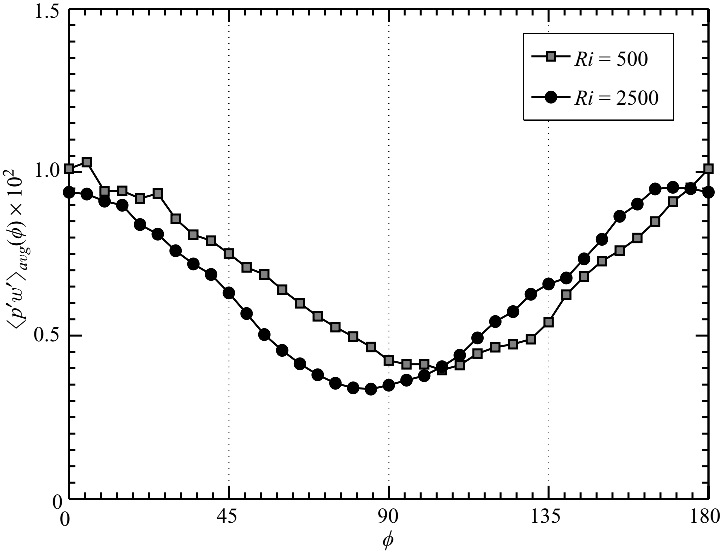

FIGURE 25. Variation of the averaged vertical energy flux normalized by $\rho_0 u^3_{\tau,max}$ over a phase for $Ri = 500$ and 2500.

7. Conclusions

We have used LES to investigate the dynamics of a stratified bottom boundary layer under an oscillating current driven by a pressure gradient that oscillates at a low frequency, 12.4 h, corresponding to a M_2 tide. A DMM is used, buoyancy-related stability functions are not necessary and the near-bottom turbulence is resolved at the moderate Reynolds number, $Re_s = 1790$, considered here. The effect of increasing the background stratification, measured by $Ri = N_\infty^2/\omega^2$, on the flow evolution is systematically studied with particular attention to the dependence on tidal phase.

The fluid has a uniform background stratification while the bottom boundary is adiabatic. A bottom mixed layer forms and grows with an entrainment rate which is reduced by the external stratification, and with a periodic modulation owing to the tidal oscillation. The mixed layer height decreases during the acceleration stage when the production of turbulence is confined to the wall region whereas, during the deceleration stage, the height increases due to the upward spread of the turbulence in response to an adverse pressure gradient. The turbulent mixed layer is separated from the stratified outer layer by a thermocline with an overshoot in temperature gradient that gradually weakens over time due to both turbulent and molecular diffusion. The turbulent heat flux has significant modulation over the tidal cycle: its depth-integrated value is low when the free-stream velocity is high and increases rapidly during the early decelerating phase.

Stratification has a strong influence on the flow statistics. When stratification increases, the range of phases where the log-law is applicable shortens, and the thickness of the log layer decreases. Stratification changes the wall stress τ_w, leading to a small increase of the friction coefficient c_f. During a portion of the tidal cycle, the mean velocity exhibits an appreciable overshoot with respect to the prevailing free-stream current and, in particular, the peak velocity exceeds the peak value of the external velocity. By examination of terms in the mean momentum equation, it is shown that the velocity overshoot is caused by the asymmetric dependence on tidal phase of the Reynolds shear stress gradient. The overshoot is intensified by stratification since the gradient of the Reynolds shear stress increases owing to the significant reduction in vertical length scale at high stratification. Stratification leads to a pronounced suppression of turbulence intensities in the outer layer although the inner, near-bottom values show little effect.

In oscillatory flow, flow statistics can have a noticeable phase lag or lead with respect to the external current. Stratification substantially changes the observed phase difference. The maximum value of the wall shear stress $\tau_{w,max}$ leads (occurs before) the maximum free-stream current by a phase of up to 25° compared to 17° when stratification is absent. TKE in the outer layer lags the current for all cases because of the increase of outer layer turbulence during the decelerating part of the cycle when an adverse pressure gradient acts on the flow. Similarly, there is considerable phase lag of turbulent production and dissipation, as much as 60° (equivalently 2 h), depending on the height above bottom. Phase lags of peak turbulent dissipation rate with comparable magnitude have been reported in field data but it is worth emphasizing that the present simulations show that the value of the lag depends critically on the measurement location with respect to the boundary layer height. The depth-integrated production and dissipation attain their peak values at approximately the same time as the external current; however, the depth-integrated buoyancy flux and TKE have a substantial phase lag.

A definition of boundary layer height based on mean velocity is difficult given the change in the shape of velocity profiles over a cycle. One definition of the turbulent boundary layer thickness δ_t is based on the location of a specific *TKE* contour, taken here to be 10 % of the maximum *TKE*. The value of $\delta_t(\phi)$ increases continuously from its minimum value in the early acceleration stage to reach a maximum during the late deceleration stage followed by an abrupt decrease corresponding to a collapse of turbulence. The value of δ_t is suppressed when stratification increases; its maximum value at $Ri = N_\infty^2/\omega^2 = 2500$ decreases to about 0.6 of the corresponding unstratified value. The turbulent boundary layer height $\delta_t(\phi)$ is found to be a suitable length scale for profiles of the outer layer statistics. The friction velocity $u_\tau(\phi)$ is found to be a good scale for the velocity statistics in both the inner and the outer layer. However, the scales, $u_\tau(\phi)$ and $\delta_t(\phi)$ cannot be used when their values approach zero.

Fine-scale turbulence is initiated close to the wall during the late acceleration phase of the cycle ($45^\circ < \phi < 90^\circ$) and achieves its maximum level during the early deceleration stage ($90^\circ < \phi < 135^\circ$). Visualizations show that, during the late deceleration stage ($135^\circ < \phi < 180^\circ$), fine-scale turbulence is advected away from the wall and larger scale eddies develop consistent with the larger intensity of the *TKE* field in the outer layer that was shown in figure 11(*a*). Thorpe *et al.* (2008) observed a similar development of large-scale eddies from fine-scale near-wall turbulence in a tidal current in a weakly stratified shallow-water region of the Irish Sea. Turbulence was found by the authors to move upwards in the form of bursts which, on reaching the sea surface, formed boils.

Turbulence in the bottom boundary layer excites internal gravity waves that propagate upwards into the overlying stratified fluid. The source of the generation of the internal waves is bounded from above by the top of the mixed layer. The tilt of the phase lines of the internal waves with respect to the vertical depends of the relative velocity of the eddies with respect to the external background current. The tilt changes as a function of phase and between near and far fields because, first, the predominant sign of the relative velocity changes with phase and, second, there is a history effect, i.e. the phase lines observed at current time are emitted from the boundary layer at a prior time when a different mean flow and state of turbulence prevails. Although broadband with $\Omega < N_\infty$ in the region above and close to the boundary layer, the internal waves span a narrower band in the far field with phase lines clustered within $40^\circ < \Theta < 62^\circ$. More energetic waves are observed during the late decelerating and the early accelerating stages of the tidal cycle. The internal wave flux is comparable to the buoyancy flux but substantially smaller than the depth-integrated turbulent dissipation or production.

We are grateful for the support provided by ONR N000140810504, program monitor Scott Harper, to B. Gayen and S. Sarkar.

REFERENCES

Akhavan, R., Kamm, R. D. & Shapiro, A. H. 1991*a* An investigation of transition to turbulence in bounded oscillatory Stokes flows. Part 1. Experiments. *J. Fluid Mech.* **225**, 395–422.

Akhavan, R., Kamm, R. D. & Shapiro, A. H. 1991*b* An investigation of transition to turbulence in bounded oscillatory Stokes flows. Part 2. Numerical simulations. *J. Fluid Mech.* **225**, 423–444.

Armenio, V. & Sarkar, S. 2002 An investigation of stably stratified turbulent channel flow using large-eddy simulation. *J. Fluid Mech.* **459**, 1–42.

Bewley, T. R. 2007 *Numerical Renaissance: Simulation, Optimization and Control*. Renaissance Press.

Blondeaux, P. & Seminara, G. 1979 Transizione incipiente al fondo di un'onda di gravitá. *Rend. fisici Accad.Lincei, serie 8* LXVII.

Burchard, H., Petersen, O. & Rippeth, T. P. 1998 Comparing the performance of the Mellor–Yamada and the κ-ϵ two-equation turbulence models. *J. Geophys. Res.* **103** (C5), 10 543–10 554.

Costamagna, P., Vittori, G. & Blondeaux, P. 2003 Coherent structures in oscillatory boundary layers. *J. Fluid. Mech.* **474**, 1–33.

Davies, A. M., Jones, J. E. & Xing, J. 1997 Review of recent developments in tidal hydrodynamic modeling. II: turbulence energy models. *J. Hydraul. Engng* **123** (4), 293–302.

Dohan, K. & Sutherland, B. R. 2003 Internal waves generated from a turbulent mixed region. *Phys. Fluids* **15** (2), 488–498.

Dohan, K. & Sutherland, B. R. 2005 Numerical and laboratory generation of internal waves from turbulence. *Dyn. Atmos. Oceans* **40**, 43–56.

Germano, M., Piomelli, U., Moin, P. & Cabot, W. H. 1991 A dynamic subgrid-scale eddy viscosity model. *Phys. Fluids* **3** (7), 1760–1765.

Hino, M., Kashiwayanagi, M., Nakayama, A. & Hara, T. 1983 Experiments on the turbulence statistics and the structure of a reciprocating oscillatory flow. *J. Fluid Mech.* **131**, 363–400.

Hino, M., Sawamoto, M. & Takasu, S. 1976 Experiments on transition to turbulence in an oscillatory pipe flow. *J. Fluid Mech.* **75**, 193–207.

Hsu, C.-T., Lu, X. & Kwan, M.-K. 2000 LES and RANS studies of oscillating flows over flat plate. *J. Engng Mech.* **126**(2), 186–193.

Jensen, B. L., Sumer, B. M. & Fredsøe, J. 1989 Turbulent oscillatory boundary layers at high Reynolds numbers. *J. Fluid Mech.* **206**, 265–297.

Klemp, J. B. & Durran, D. R. 1983 An upper boundary condition permitting internal gravity wave radiation in numerical mesoscale models. *Mon. Weather Rev.* **111**, 430–444.

Lighthill, J. 1990 *Waves in Fluids*, 1st edn. Cambridge University Press.

Lohmann, I. P., Fredsøe, J., Sumer, B. M. & Christensen, E. D. 2006 Large eddy simulation of the ventilated wave boundary layer. *J. Geophys. Res. – Oceans* **111**, C06036.

Lorke, A., Umlauf, L., Jonas, T. & Wüest, A. 2002 Dynamics of turbulence in low-speed oscillating bottom-boundary layers of stratified basins. *Environ. Fluid Mech.* **2**, 291–313.

Lozovatsky, I., Liu, Z., Wei, H. & Fernando, H. J. S. 2008*a* Tides and mixing in the northwestern East China Sea. Part I: rotating and reversing tidal flows. *Cont. Shelf Res.* **28**, 318–337.

Lozovatsky, I., Liu, Z., Wei, H. & Fernando, H. J. S. 2008*b* Tides and mixing in the northwestern East China Sea. Part II: near-bottom turbulence. *Cont. Shelf Res.* **28**, 338–350.

Lund, T. S. 1997 On the use of discrete filters for large eddy simulation. In *Annual Research Briefs*, pp. 83–95. Center for Turbulence Research, NASA Ames/Stanford University.

Luznik, L., Gurka, R., Nimmo Smith, W. A. M., Zhu, W., Katz, J. & Osborn, T. R. 2007 Distribution of energy spectra, Reynolds stresses, turbulence production and dissipation in a tidally driven boundary layer. *J. Phys. Oceanogr.* **37**, 1527–1550.

Nagaosa, R. & Saito, T. 1997 Turbulence structure and scalar transfer in stably stratified free-surface flows. *AIChE J.* **43**, 2393.

Perlin, A., Moum, J., Klymak, J., Levine, M., Boyd, T. & Kosro, P. 2005 A modified law-of-the-wall applied to oceanic bottom boundary layers. *J. Geophys. Res.* **110**, C10S10, doi: 10.1029/2004JC002310.

Perlin, A., Moum, J., Klymak, J., Levine, M., Boyd, T. & Kosro, P. 2007 Organization of stratification, turbulence, and veering in bottom Ekman layers. *J. Geophys. Res.* **112**, C5, doi: 10.1029/2004JC002641.

Radhakrishnan, S. & Piomelli, U. 2008 Large-eddy simulation of oscillating boundary layers: model comparison and validation. *J. Geophys. Res.* **113**, C02022.

Richards, K. J. 1982 Modeling the benthic boundary layer. *J. Phys. Oceanogr.* **12**, 428–439.

Sakamoto, K. & Akitomo, K. 2006 Instabilities of the tidally induced bottom bottom boundary layer in the rotating frame and their mixing effect. *Dyn. Atmos. Oceans* **41**, 191–211.

Sakamoto, K. & Akitomo, K. 2008 The tidally induced bottom boundary layer in a rotating frame: similarity of turbulence. *J. Fluid Mech.* **615**, 1–25.

Sakamoto, K. & Akitomo, K. 2009 The tidally induced bottom boundary layer in the rotating frame: development of the turbulent mixed layer under stratification. *J. Fluid Mech.* **619**, 235–259.

Salon, S., Armenio, V. & Crise, A. 2007 A numerical investigation of the Stokes boundary layer in the turbulent regime. *J. Fluid Mech.* **570**, 253–296.

Sarpkaya, T. 1993 Coherent structures in oscillatory boundary layers. *J. Fluid Mech.* **253**, 105–140.

Scotti, A. & Piomelli, U. 2001 Numerical simulation of pulsating turbulent channel flow. *Phys. Fluids* **13** (5), 1367–1384.

Sleath, J. F. A. 1987 Turbulent oscillatory flow over rough beds. *J. Fluid. Mech.* **182**, 369–409.

Spalart, P. R. & Baldwin, B. S. 1987 Direct simulation of a turbulent oscillating boundary layer. In *Turbulent Shear Flows* (eds. J.-C. Andre, J. Cousteix, F. Durst, B. E. Launder, F. W. Schmidt & J. H. Whitelaw), vol. 6, pp. 417–440. Springer.

Sutherland, B. R. & Linden, P. F. 1998 Internal wave excitation from stratified flow over a thin barrier. *J. Fluid Mech.* **377**, 223–252.

Taylor, J. R. & Sarkar, S. 2007 Internal gravity waves generated by a turbulent bottom Ekman layer. *J. Fluid Mech.* **590** (1), 331–354.

Taylor, J. R. & Sarkar, S. 2008 Stratification effects in a bottom Ekman layer. *J. Phys. Oceanogr.* **38** (11), 2535–2555.

Taylor, J. R., Sarkar, S. & Armenio, V. 2005 Large-eddy simulation of stably stratified open channel flow. *Phys. Fluids* **17**, 116602.

Thorpe, S. A., Green, J. A. M., Simpson, J. H., Osborn, T. R. & Nimmo Smith, W. A. M. 2008 Boils and turbulence in a weakly stratified shallow tidal sea. *J. Phys. Oceanogr.* **38**, 1711–1730.

Vittori, G. & Verzicco, R. 1998 Direct simulation of transition in an oscillatory boundary layer. *J. Fluid Mech.* **371**, 207–232.

Vreman, B., Geurts, B. & Kuerten, H. 1997 Large-eddy simulation of the turbulent mixing layer. *J. Fluid Mech.* **339**, 357–390.

Zang, Y., Street, R. L. & Koseff, J. R. 1993 A dynamic mixed subgrid-scale model and its application to turbulent recirculating flows. *Phys. Fluids* A **5** (12), 3186–3196.